Search for zonal flows in the edge turbulence of Alcator C-Mod

2012 Plasma Phys. Control. Fusion 54 025008

(http://iopscience.iop.org/0741-3335/54/2/025008)

Plasma Phys. Control. Fusion **54** (2012) 025008 (21pp) doi:10.1088/0741-3335/54/2/025008

Search for zonal flows in the edge turbulence of Alcator C-Mod

S J Zweben[1], J L Terry[2], M Agostini[3], R Hager[4], J W Hughes[2], J R Myra[5], D C Pace[6] and the Alcator C-Mod Group

[1] Princeton Plasma Physics Laboratory, Princeton NJ 08540, USA
[2] Massachusetts Institute of Technology, Cambridge MA 02139, USA
[3] Consorzio RFX, Associazione EURATOM, I-35127, Padova, Italy
[4] Max Planck Institute for Plasma Physics, D-85748 Garching, Germany
[5] Lodestar Research Corporation, 2400 Central Ave., Boulder CO 80301, USA
[6] ORISE, Oak Ridge, TN 37831, USA

E-mail: szweben@pppl.gov

Received 29 September 2011, in final form 2 December 2011
Published 19 January 2012
Online at stacks.iop.org/PPCF/54/025008

Abstract
The time-dependent radial and poloidal velocity of edge turbulence is evaluated using a 2D time-delayed cross-correlation analysis of fast camera data from the gas puff imaging (GPI) diagnostic viewing the outer midplane region in Alcator C-Mod. The local poloidal velocity fluctuations are averaged over the poloidal viewing region of the GPI diagnostic and radially resolved over ±2 cm around the separatrix. The resulting poloidal velocity usually has a broadband frequency spectrum in the range ∼1–20 kHz, and a radial correlation width which decreases with increasing line-averaged density. In some cases with ICRH heating there was also a coherent poloidal velocity oscillation at 6–7 kHz which was highly correlated with a poloidal magnetic field oscillation at the same frequency. Some of these results are similar to the geodesic acoustic modes and/or zonal flows described in previous experiments and theory.

(Some figures may appear in colour only in the online journal)

1. Introduction

The velocity of edge turbulence in tokamaks is an important factor in determining the plasma parameters of the edge and scrape-off layer (SOL). The radial motion of turbulence is generally considered to be the dominant cause of edge transport [1–3], and the poloidal motion can in theory control the turbulence level *via* mean or time-dependent zonal flows or geodesic acoustic modes (GAMs) [4–8]. Therefore, it is important to measure both the radial and poloidal motion of turbulence in order to understand the physics of the cross-field transport in the edge and SOL of tokamaks.

This paper describes time-resolved measurements of the radial and poloidal velocity of edge turbulence in Alcator C-Mod made using a gas puff imaging (GPI) diagnostic, which can measure edge turbulence within a radial range about ±2 cm near the outer midplane separatrix. This imaging data were taken at an upgraded speed of 391 000 frames s^{-1}, and the 2D cross-correlation analysis method used here is capable of resolving turbulence velocity fluctuations up to about 30 kHz.

The main goal of this paper was to search for the presence of time-dependent poloidal zonal flows in the GPI data by averaging the local velocity measurements over the available poloidal field of view. This goal was motivated by recent measurements of edge zonal flows and/or GAMs in the frequency range ∼5–20 kHz, as reviewed in [5–8]. Many of these measurements have been made locally within a single poloidal/toroidal region [9–19], while others have used two widely separated detectors to confirm the global structure of these flows [20–26]. Various types of diagnostic techniques have been used; for example, heavy ion beam probes in CHS [20], Langmuir probes in T-10 [21], beam emission spectroscopy (BES) in DIII-D [9] and microwave Doppler reflectometry in ASDEX Upgrade [12].

In general, two types of zonal flows have been identified: a coherent oscillation identified with the theoretically predicted GAM, and broadband fluctuations identified with 'zero-mean frequency' zonal flows. Thus the primary goal of this work was to search for the presence of such GAMs or zonal flows in C-Mod, where they have not been seen previously. The present

GPI measurements were localized near the outer midplane, so only the local, and not the global, structure of the poloidal flows can be directly measured.

A second motivation for this work was to learn more about the radial velocity of the edge turbulence, since this can directly affect the radial transport. The time-averaged convective velocity of edge turbulence was previously measured in C-Mod using GPI data [27–31], but time-dependent velocity fluctuations were not evaluated. Local radial turbulence velocity fluctuations have been measured with probes in many other tokamaks [1–3], e.g. in DIII-D [32] and JET [33], but the poloidally averaged radial velocities have not been measured. Thus the secondary goal of this paper is to evaluate the poloidally averaged radial velocity fluctuations from the GPI data and compare them with the poloidal velocity fluctuations (also poloidal-averaged), and with the time-averaged radial velocities determined from the same data.

The organization of this paper is as follows: the GPI diagnostic and data analysis technique is described in section 2, the parameters of Alcator C-Mod and the database used here is described in section 3, and the results of this analysis are described in section 4. A summary and discussion of the results, including comparisons with previous experiments and theory, is given in section 5, along with conclusions and suggestions for further work.

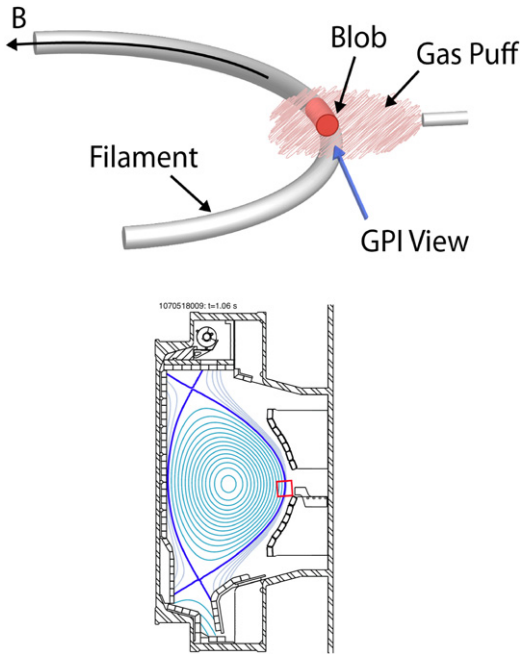

Figure 1. Schematic illustration of the GPI diagnostic geometry (top), and the location of the GPI camera field of view near the outer midplane in the present experiment (bottom box). The GPI diagnostic measures the D_α or He I light emitted by a neutral gas cloud as viewed along the local B field direction, in order to image the 3D turbulence filament in the radial versus poloidal plane perpendicular to B.

2. Diagnostic description and data analysis

This section describes the GPI diagnostic and data analysis: section 2.1 describes the GPI diagnostic techniques, section 2.2 describes the data processing and backgrounds, section 2.3 discusses the interpretation of GPI signals and section 2.4 describes the data analysis methods used in this paper.

2.1. GPI diagnostic

The GPI technique has been described previously [27–31] so only a brief description emphasizing the new features will be given here. The GPI diagnostic uses the plasma-induced excitation of the neutral deuterium D_α (656.3 nm) or helium He I (587.6 nm) line emission to measure the local 2D structure and motion of the edge turbulence in the plane perpendicular to the local magnetic field B, as illustrated in figure 1. The diagnostic region used in the present experiment covers a ∼5.5 cm radial by ∼5.5 cm poloidal region near the outer midplane separatrix, shown by the small box at the bottom of figure 1), which is viewed along the local B field at ∼11° with respect to the toroidal direction. The gas cloud is used to spatially localize the D_α or He I line emission along this sightline, so that the local turbulence structures perpendicular to B within the gas cloud can be well resolved.

The D_2 or He gas puff is introduced by a set of four mm-sized holes in a manifold in the limiter shadow near the region to be imaged. The GPI gas cloud is viewed by a telescope mounted on the outer wall ∼50 cm away, and the resulting image is transferred through a vacuum window to a custom-made 5 m long 57 × 57 quartz fiber imaging bundle. Prior experiments used glass fiber optic bundles which were replaced in 2009 due to radiation darkening, most likely due to the high x-ray fluxes generated in C-Mod. The strength of the D_2 GPI puff can be adjusted to give a D_α signal level at least five times larger than the D_α background level just before the GPI puff. For the cases with a He GPI puff into deuterium plasmas, the signal level of He I with the puff is much more than ten times higher than the background level before the GPI puff.

The image at the other end of the fiber bundle is passed through a D_α or He I filter, and viewed by a Phantom 710 camera from Vision Research, Inc. For all experiments described in this paper the camera was operated at 391 000 frames s^{-1} with an exposure time of 2.2 μs/frame. This is faster than previous cameras used on C-Mod, which were operated at 250 000 frames s^{-1} [27–31]. The images for this paper were digitized at 64 × 64 pixels/frame with a 12 bit dynamic range for at least 30 000 frames/shot (i.e. 75 ms/shot) just before and during the GPI gas puff.

The spatial resolution of the optical system is ∼2–3 mm at the gas cloud, which is smaller than the typical turbulence size scale of ∼5–10 mm. The spatial resolution of the turbulence also depends on the extent of the localization of the 3D turbulence filament by the gas cloud, which in turn depends on the signal/background ratio, as described in the following section. The time between frames is ∼2.5 μs, which is short enough to capture almost all of the fluctuation power spectrum. There was also a separate array of views coupled to individual diode detectors which viewed the same gas cloud at an angle of 0° with respect to the toroidal direction [30] with a higher bandwidth but lower spatial resolution. Data from that diode array are not used in this paper.

2.2. Data processing and backgrounds

The data for each shot in the present experiment were analyzed for a 20 ms long period near the peak of the GPI puff when the gas puffing rate and GPI signal level were approximately constant. The raw camera images for each frame were first normalized to a single 20 ms time-averaged frame for that shot, in order to eliminate systematic pixel-to-pixel spatial variations due to the fiber bundle and optics. The resulting images show a smoothly varying space-time structure which clearly resolves the motion of the turbulence, at least on a spatial scale ~0.5–5 cm. These images can be seen in sample videos [34].

For the GPI measurements made using D_α, the main background is due to wall recycling of deuterium outside the GPI puff but within the GPI field of view. Since these background neutrals are roughly uniformly distributed toroidally, the background contains the full 3D structure of the B-field-aligned edge turbulence filaments within the GPI field of view (see figure 1). Thus this background appears in the 2D images as radially elongated 'hoops' connected to each bright turbulence blob. Since this 3D background effect is also fluctuating, it cannot easily be subtracted out. The effect of this background was minimized by increasing the D_2 GPI puff strength until the signal/background ratio was ~5 or more near the separatrix. This is large enough so that the local 2D structure of the turbulence in the SOL is clearly resolved up to 1–2 cm inside the local separatrix. Farther inside this radius the D_α signal level due to the GPI puff decreases rapidly, so that the radial structure and motion of the local turbulence cannot be clearly resolved. This 3D background effect is negligible when the GPI puff gas is He and the He I line is used.

2.3. Interpretation of GPI signals

The interpretation of GPI signals has been discussed previously based on DEGAS 2 modeling of the neutral gas puff and atomic physics of D_α [35] and He I [36]. The light emission in these lines is proportional to $n_o f(n_e, T_e)$, where n_o is the local neutral density and $f \sim n_e^\alpha T_e^\beta$, where typically $\alpha, \beta \sim 0.5$–1.0 near the spatial peak of the GPI signal in C-Mod. Good agreement was obtained between the calculated and measured radial location of the time-averaged light emission from these lines, given the measured density and temperature profiles in C-Mod [35] and NSTX [36]. Atomic physics calculations indicated the response time of these lines to changes in n_e or T_e should be $\leqslant 1\ \mu$s.

Thus the local fluctuations in GPI light emission are non-linear functions of the local density and temperature fluctuations, assuming that the neutral density from the gas puff does not vary on the timescale of the turbulence. It was shown previously that this nonlinearity does not significantly affect the cross-correlation properties of the turbulence [37], i.e. the correlation lengths and correlation times are largely independent of α, β. These nonlinearities act like the contrast control of a TV monitor, in that they change the relative brightness but not the structure or motion of objects. However, the relative GPI fluctuation level does retain a sensitivity to these nonlinearities, and so is not the same as the relative density fluctuation level. The interpretation of GPI signals does assume a correlation between the local electron density and temperature, since if these were uncorrelated the resulting line emission would be a mixture of the two time dependences. However, theoretical simulations of the C-Mod SOL plasma have shown a high correlation between n_e and T_e [38], as expected for $E \times B$ advection.

The interpretation of the 2D GPI image sequences in terms of 2D turbulence velocities has been discussed previously for both time-averaged analyses in C-Mod [27–31] and time-dependent analyses in NSTX [17, 18]. The time-delayed cross-correlation analysis used in this paper (section 2.4) works best when these complicated structures move less than their scale size L_{pol} within a frame-to-frame time, i.e. for the present case when their velocity is $V \leqslant 0.8\,\text{cm}/2.5\,\mu\text{s} \sim 3\,\text{km s}^{-1}$. The natural unit for this velocity analysis is 1 pixel/frame or $V \sim 0.34\,\text{km s}^{-1}$ for the present cases, but averaging over many pixels or frames can resolve velocities significantly lower than this.

There are some additional limitations on the interpretation of the present 2D GPI image sequences in terms of 2D velocities versus time. For example, motion along a direction in which there is no signal gradient cannot be detected at all, and the cross-correlation technique used here tends to weight the most intense structures and to miss the weaker or smaller-scale ones. These limitations are discussed for GPI velocity analysis in [39] and for the similar time delay estimation method for BES data in [40]. There are also fundamental limitations in interpreting the turbulence velocity in terms of local fluid velocity, as discussed in section 5.2.

2.4. Velocity analysis using 2D cross-correlations

The turbulence velocity was estimated for these experiments using a time-resolved 2D cross-correlation analysis code similar to the one used previously to evaluate poloidal flows in GPI data from NSTX [17]. This technique is also similar to the time delay estimation method previously used to evaluate zonal flows from BES turbulence data in DIII-D [9, 14]. The present analysis aims to search for large-scale fluctuating poloidal flows in the GPI data; thus, once the local velocities for each pixel are found, they are averaged over the poloidal field of view to evaluate (as well as possible) the large-scale zonal flow component of these velocities.

The first step in the analysis is to normalize each 64 × 64 frame from the GPI camera to the time-averaged frame, as described in section 2.2. Two examples of such frames are illustrated in figure 2, where the separatrix is shown by a dashed line, the limiter shadow by a dotted line, and the 5.5 cm × 5.5 cm frame was oriented so that radially outward is to the right, and the poloidal ion diamagnetic and grad-B drift directions are downward. The next step is to choose a single pixel within the analysis region defined by the black box in figure 2 (pixels 20–50 horizontally and 8–55 vertically). Then for this pixel for this frame, a short time series is created consisting of the normalized intensities at that pixel for a time period ±5 frames around the initial frame, i.e. a time series is formed with a length of 10 frames ×2.5 μs = 25 μs. Then a cross-correlation of this time series is done with a second

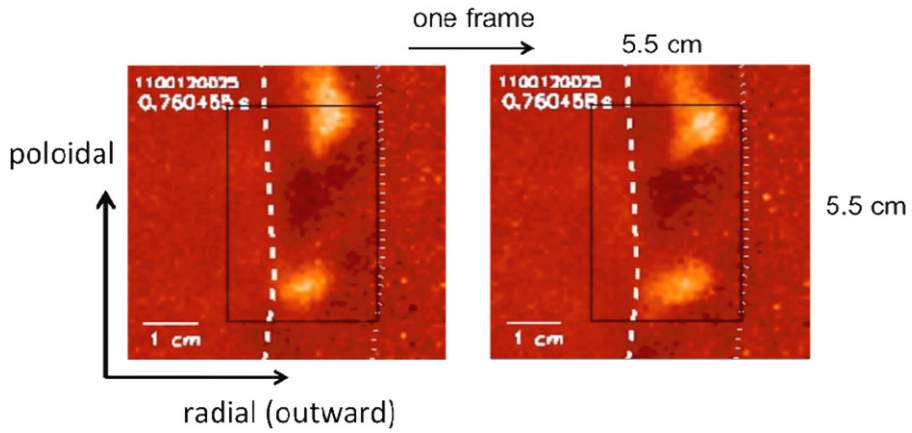

Figure 2. Example of two successive normalized frames separated by 2.5 μs, each with an exposure time of 2.2 μs. The signal level is shown in a false color scale (white as maximum), the separatrix is the dashed white line, the limiter shadow is shown by the dotted white line, and the black box is the data analysis region.

time series (of the same duration) for each of the neighboring ± 8 pixels in 2D, but centered on the *following* time frame. Then the *spatial location* of the maximum cross-correlation coefficient between the initial pixel's time series with the time series in the next frame is found. This locates the place where the fluctuations in the initial pixel are best correlated with the fluctuations in the following frame, i.e. this finds the local motion of the turbulence between these two frames.

The spatial location of this maximum cross-correlation coefficient is then evaluated for each pixel in every frame. The radial and poloidal velocities for each pixel are then found from the horizontal and vertical displacements between the initial pixel and the pixel with the maximum cross-correlation in the next frame, using the calibration 1 pixel/frame $=$ 0.34 km s^{-1}. This analysis requires correlating $\sim 30 \times 47$ pixels over 16×16 neighboring points for each time step, i.e. ~ 2 billion correlations for a typical 20 ms analysis.

Finally, the poloidal and radial velocities for each pixel for each frame are poloidally averaged over each ~ 4 cm poloidal high column in the analysis region of figure 2 in order to estimate the 'zonal flows' in this region. Although this process is only an approximation to the ideal $m = 0$ poloidal structure of these flows, it is the best that can be done to evaluate the zonal flow component with the limited poloidal range of this diagnostic (see section 5.2). A qualitatively similar local poloidal velocity analysis was used to identify zonal flows in [9–19].

The search for the maximum cross-correlation is limited to ± 8 pixels vertically (in the poloidal direction), which corresponds to a maximum detectable poloidal velocity of 8 pixels/frame ~ 2.7 km s^{-1} in either direction. This search range therefore limits the poloidal averaging region of the results, since we cannot search outside the 64×64 frame. The choice of ± 8 pixels was a compromise between having a reasonably large 4 cm poloidal averaging region, and having a reasonably large range of detectable velocities. The radial search range was bounded by the limiter shadow at the outside, and by the diminishing GPI signal on the inside. The resulting poloidally averaged poloidal and radial velocities were almost always $\leqslant 1$ km s^{-1}, although individual pixels were sometimes at the ~ 2.7 km s^{-1} limit of this poloidal velocity range. A typical maximum cross-correlation coefficient from this velocity analysis procedure was 0.8, i.e. the turbulence structure largely moved as a 'frozen flow' over the 2.5 μs time delay between frames.

An example of this analysis technique for measuring the poloidal velocity is shown at the top left of figure 3. In this case the $V_{\rm pol}$ estimated for one column of pixels (at $\rho = 0.64$ cm) and for one time (0.752 561 s) is plotted as a function of the poloidal position (i.e. vertical pixel) over a range of about ± 2 cm in the analysis box of figure 2. The typical $V_{\rm pol}$ is in the range ± 1 km s^{-1}, although there is a significant variation of $V_{\rm pol}$ with vertical position, which is not surprising due to the turbulent nature of the flow. For the rest of the analysis in this paper, *only the poloidal average of the poloidal velocity over the analysis box* of figure 2 will be used, which is illustrated for this case by the dashed line at the top of figure 3. This is used to evaluate the zonal flow in this region. Some discussion of the limitations of this analysis is in section 5.2.

The radial profile of the poloidally averaged $V_{\rm pol}$ for this same time frame is shown by the solid line at the upper right of figure 3, and the 20 ms time-averaged profile of this poloidally averaged radial profile of $V_{\rm pol}$ is shown by the dashed line. There is a significant radial variation of $V_{\rm pol}$ over the radial range $-1\,{\rm cm} \leqslant \rho \leqslant 2\,{\rm cm}$, which is the radial range of the analysis box for this case. Sample time dependences of the poloidally averaged $V_{\rm pol}$ and $V_{\rm rad}$ are shown for a 1.2 ms (500 frame) interval at the bottom left of figure 3. The time-averaged radial velocity at this radius ($\rho = 0.32$ cm) is $V_{\rm rad} \sim 0.5$ km s^{-1} (radially outward), while the time-averaged poloidal velocity is $V_{\rm pol} \sim -1$ km s^{-1} (in the ion diamagnetic direction). The time-average of these time-dependent velocities agreed well with the time-average velocity obtained using cross-correlations made over a long (~ 10 ms) time series [29].

This time-dependent velocity analysis was checked by taking a typical frame of GPI data and artificially oscillating it vertically and horizontally in a square-wave motion with various speeds and periods as a function time. The relative frequency response to this motion was ~ 30 kHz (to 1/e

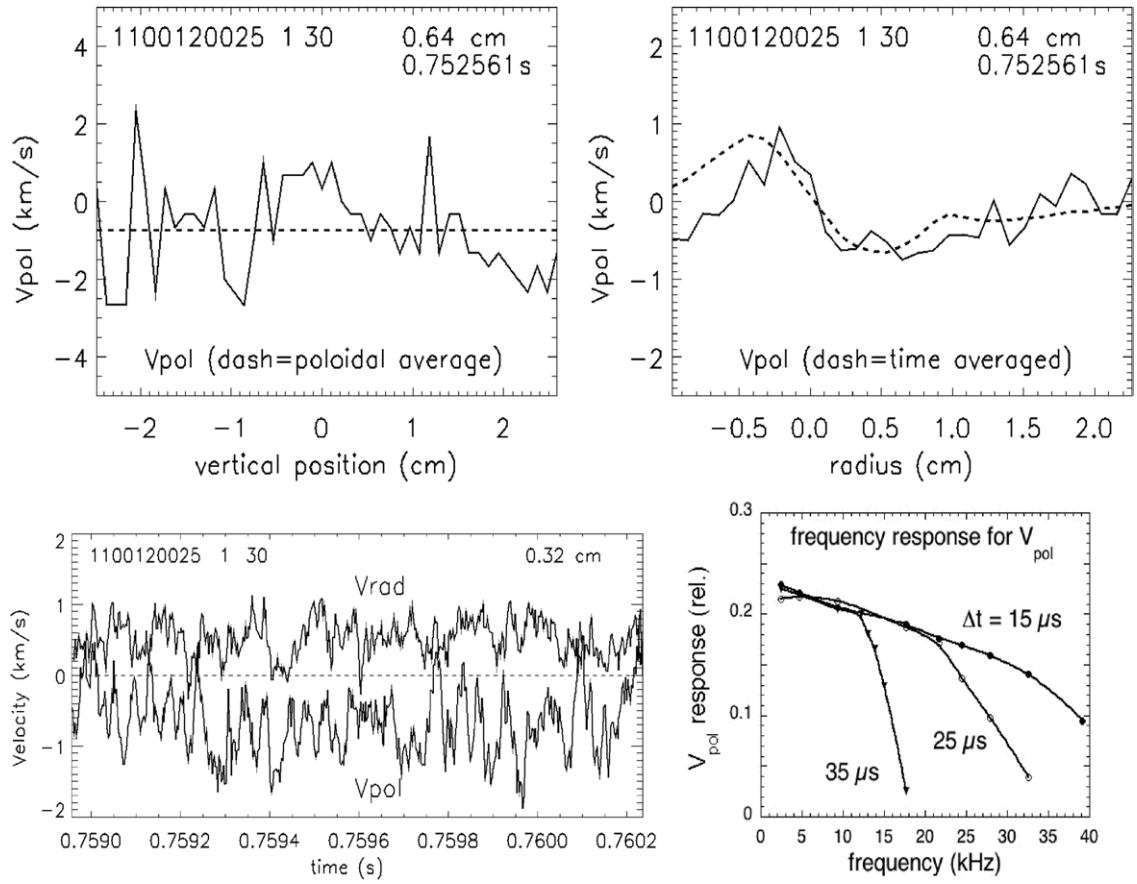

Figure 3. Example of a cross-correlation analysis for the poloidal velocity. At the upper left is the local V_{pol} versus the vertical pixel (poloidal coordinate) inferred for one radius for one frame, and the poloidally averaged V_{pol} (dashed). At the upper right is the radial profile of the poloidally averaged V_{pol} for one frame, and also the 20 ms time-averaged V_{pol} (dashed). At the lower left are typical poloidally averaged V_{pol} and V_{rad} versus time for a single radius (i.e. vertical column of pixels). At the lower right is the relative frequency response of this analysis to an artificial square-wave velocity imposed on this turbulence. The three curves are for different durations of time sampling used to cross-correlate the data, where $\Delta t = 25\,\mu$s was used in the analyses of this paper.

amplitude), which was set by the 25 μs length of the time series used in the cross-correlation analysis, as shown at the bottom right of figure 3. The frequency spectra of fluctuations in these velocities will be discussed in section 4.

3. Database and edge turbulence characteristics

This section describes the C-Mod database used for this experiment in section 3.1, the edge turbulence characteristics in section 3.2, and the edge plasma characteristics in section 3.3. Since these edge turbulence characteristics are similar to those described previously for GPI measurements in C-Mod [27–31], they will not be discussed in detail. The turbulence velocity analysis is in section 4.

3.1. Database for this analysis

The data used for this paper were all taken during the C-Mod 2009-2011 run periods using the midplane GPI camera running at 391 000 frames s^{-1}. The GPI field of view remained constant with respect to the vessel during this period, although the separatrix location varied from shot to shot within this field of view. All discharges were standard lower single-null diverted deuterium plasmas with a nominal size of $R_o = 0.67$ m and $a = 0.23$ m.

The list of the 30 discharges used in this paper is shown in table 1. The primary criterion for the selection of these shots was the quality of the GPI data. This required that the GPI signal level during the GPI gas puff was $\geqslant$5 times the background level before the GPI puff, so that the fluctuations were well localized along the line of sight (see section 2.2). Also, these shots were selected to have $q_{95} = 3.4 \pm 0.4$ in order for the local B field to be within $\pm 2^\circ$ of the GPI sightline angle to optimally resolve the 2D turbulence structure. All GPI data for these 30 shots was taken during the steady-state portion of normal C-Mod discharges (the 31st shot was just before an L–H transition). The shots highlighted in bold in table 1 were chosen as a sample of this dataset used for subsequent illustrations, which both included cases with and without clear zonal flows in the GPI analysis.

The range of plasma parameters was $I = 0.75$–1.1 MA, $B = 3.6$–6.1 T, line-averaged density $\langle n \rangle \sim (0.7$–$1.9) \times 10^{20}$ m^{-3} (i.e. $n_G \sim 0.10$–0.35), and stored energy $W = 21$–76 kJ. Most discharges were Ohmic, but a few shots had up to $P_{RF} \sim 2$ MW of auxiliary ICRF power. The outer midplane separatrix location R_{sep} shown in table 1 varied

Table 1. Shot list.

Shot	Time (s)	I_p (MA)	B(T)	$\langle n \rangle 10^{20}$ m^{-3}	W (kJ)	P_{RF} MW)	R_{sep} (m)	GPI gas	V_{pol} width (cm)
1091216028	1.41	1.0	5.2	1.4	46	0	0.891	D	0.47
1091216029	1.41	1.0	5.2	1.2	41	0	0.892	D	0.50
1091216030	**1.41**	**1.0**	**5.2**	**1.1**	**38**	**0**	**0.893**	**D**	**0.50**
1100120006	0.76	1.0	5.4	1.1	43	0	0.886	D	0.47
1100120008	0.76	1.0	5.4	1.1	41	0	0.887	D	0.38
1100120025	**0.76**	**0.8**	**3.6**	**0.8**	**21**	**0**	**0.886**	**D**	**0.78**
1100120026	0.76	0.8	3.6	0.8	22	0	0.886	D	0.92
1100120027	0.76	0.8	3.6	0.8	22	0	0.887	D	0.81
1100721010	1.25	1.1	5.4	1.1	36	0	0.893	D	0.48
1100721011	1.25	1.1	5.4	1.2	48	0	0.895	D	0.47
1100721012	1.25	1.1	5.4	1.3	43	0	0.894	D	0.45
1100721014	1.25	1.1	5.4	1.2	37	0	0.895	D	0.50
1100803008	1.26	0.8	4.1	1.1	27	0	0.898	He	0.90
1100803015	1.26	0.8	4.1	1.6	28	0	0.899	He	0.23
1100803020	1.26	0.8	4.1	1.7	21	0	0.899	He	0.19
1100803022	1.26	1.0	5.4	1.6	36	0	0.900	He	0.15
1100824014	1.07	0.9	5.4	1.6	43	0.6	0.893	D	0.64
1100824015	1.07	0.9	5.4	1.6	47	0.8	0.893	D	0.62
1100824017	**1.07**	**1.1**	**5.4**	**1.8**	**57**	**0**	**0.893**	**He**	**0.11**
1100824019	1.07	1.1	5.4	1.9	51	0	0.894	He	0.11
1100824021	1.07	1.1	5.4	1.7	47	0	0.895	He	0.13
1100824023	1.07	1.1	5.4	1.7	45	0	0.895	He	0.24
1100824024	1.07	1.1	5.4	1.8	53	0	0.894	He	0.11
1100824025	1.07	1.1	5.4	1.8	49	0	0.893	He	0.11
1100824026	1.07	1.1	5.4	1.7	46	0	0.893	He	0.13
1100824028	1.07	1.1	6.1	1.7	39	0	0.895	He	0.13
1100824029	1.07	1.1	6.1	1.4	30	0	0.897	He	0.16
1110114023	0.91	1.0	5.3	0.8	76	1.9	0.895	D	0.76
1110114026	**0.91**	**1.0**	**5.3**	**0.7**	**60**	**1.6**	**0.895**	**D**	**0.88**
1110114027	0.91	1.0	5.3	0.7	58	1.8	0.896	D	0.87
1110114032	*0.91*	*0.9*	*4.6*	*0.7*	*58*	*1.8*	*0.894*	*D*	*2.14*

from ∼0.5–2.0 cm inside the outer limiter shadow location at $R_{lim} = 0.905$ m, and the GPI gas puff and optical filter were either D_α (656.3 nm) or He I (587.6 nm). The width of the poloidal velocity fluctuation scale length is shown in the right column of table 1 (see section 4.4).

All 30 of these discharges were in L-mode, but one shot (the last of table 1) had an L–H transition shortly after the time of analysis. This case (1110114032) is discussed separately in section 4.7. These 30 discharges covered six run days of GPI operation, with 17 shots done using the D_2 GPI puff and D_α filter, and 13 shots done using the He GPI puff and He I filter. The only significant difference between the results for these two GPI gases was the lower background level for the He GPI cases; otherwise, the turbulence characteristics are essentially the same for either GPI gas for similar discharges.

3.2. Edge turbulence characteristics

As mentioned above, the general characteristics of edge and SOL turbulence in this database are similar to those described previously for C-Mod [27–31]. Therefore in this section we just give a few examples of these characteristics in order to put the velocity analyses of section 4 into context. All analyses in this sub-section are averaged over the 4 cm poloidal (i.e. vertical) range of interest as shown by the box in figure 2, and over a 20 ms time interval (∼7800 frames) during the steady-state part of these discharges.

Figure 4 shows the radial and poloidal GPI correlation lengths evaluated for the top 30 shots in table 1 at a radial location $\rho \sim 0.5$ cm outside the separatrix. Here ρ is the radial distance from the separatrix as measured in the GPI field of view near the outer midplane (positive ρ is in the SOL). These GPI correlation lengths were first evaluated locally for each point (assuming a Gaussian cross-correction fall-off), and then averaged over the poloidal analysis region shown in figure 2. These radial and poloidal correlation lengths are almost all within the range $L_{rad} \sim L_{pol} \sim 0.8 \pm 0.3$ cm (FWHM). Thus there are about five poloidal correlations lengths within the 4 cm poloidal analysis region of figure 2. There was no systematic difference in correlation lengths measured with D or He GPI in this database (the four shots with a somewhat higher radial correlation lengths of $L_{rad} \sim 1.2$ cm were in D, i.e. 1100721010-014). There was also no strong dependence of these correlation lengths on the plasma current (at $q_{95} = 3.4 \pm 0.4$), as was also the case in [29], or on the stored energy. There was a slight decrease in correlation lengths with increasing line-averaged density, or with the Greenwald density over this range ($n_G = 0.10$–0.35). In a separate analysis of a different set of data [31] there were significant changes in the turbulence near the density limit at $n_G \geqslant 0.6$, which was not within the present database.

Figure 5 shows the radial profiles of some edge turbulence quantities for the four sample shots highlighted in table 1.

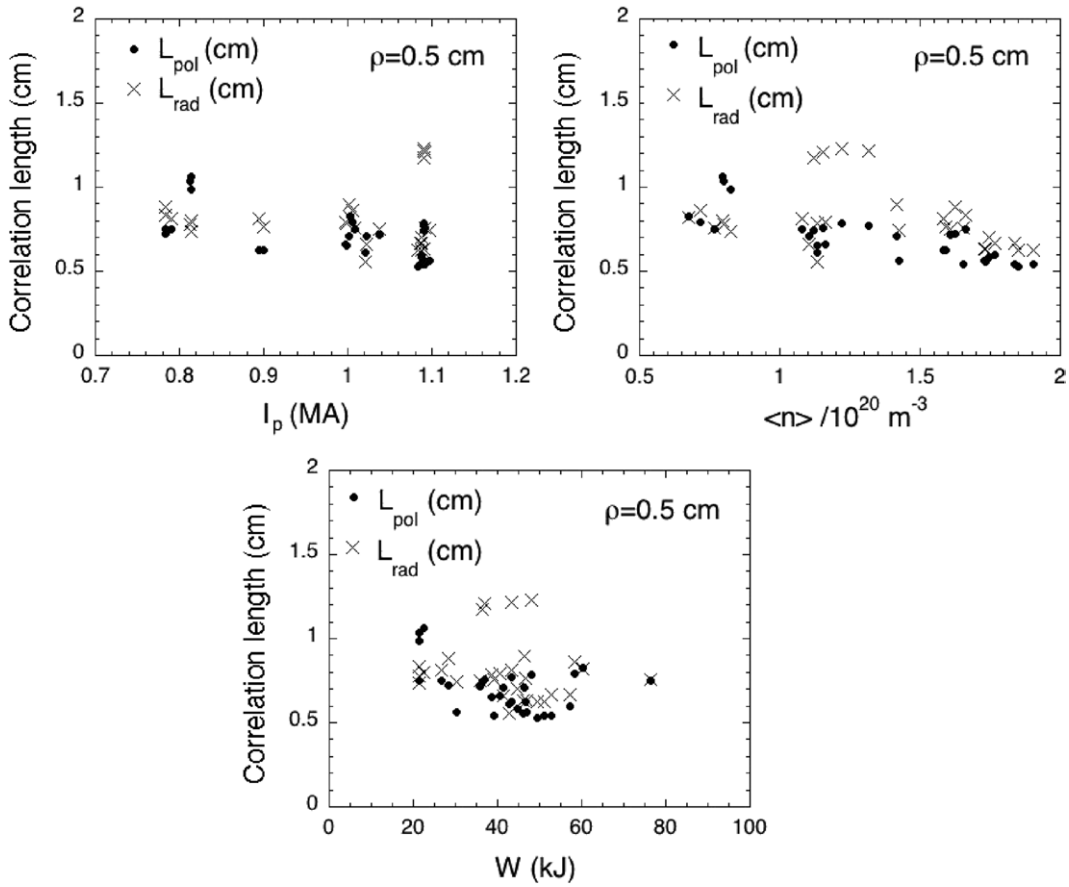

Figure 4. Radial and poloidal GPI correlation lengths for the 30 shots in this database, all evaluated at $\rho = 0.5$ cm outside the separatrix. There are only small variations in correlation length over the range of plasma current I_p, line-averaged density $\langle n \rangle$, and plasma stored energy W in this database (all with $q_{95} \sim 3.4 \pm 0.4$). There is a slight trend for smaller correlation lengths at higher density.

At the top left are the radial profiles of the relative GPI signal intensity, showing a peak within about ±0.5 cm of the separatrix (the separatrix was determined by EFIT and is judged to be uncertain by ∼0.3 cm). The relative GPI fluctuation levels $\delta I/I$ (RMS/mean) are shown for these same shots at the bottom left, and generally increase monotonically from $\delta I/I \sim 0.05$–0.2 at $\rho \sim -1.0$ cm (inside the separatrix) to $\delta I/I \sim 0.2$–0.6 at $\rho \sim 1.0$ cm (outside the separatrix), as usual for tokamak edge plasmas [1–3]. Also shown in figure 5 for these four shots are radial profiles of the radial and poloidal correlation lengths L_{rad} and L_{pol}, which are in the range $L \sim 0.5$–1.0 cm (FWHM) in almost all cases. At the top right are the profiles of the autocorrelation time, which are in the range $\tau_{auto} \sim 3$–$40\ \mu$s (FWHM), and at the bottom right are the maximum values of the cross-correlation coefficients used for the velocity analysis, which were all ∼0.8, indicating that the flow was largely 'frozen' between two frames.

3.3. Edge plasma characteristics

Edge Thomson scattering data were available for most of the shots of table 1, and a summary of the typical edge electron densities and temperatures is shown in table 2. Each number in this table is averaged over 3–4 similar shots and over a radial range of ±0.3 cm around the chosen radii of $\rho = 0$ and ±0.5 cm, with error bars from the variation in n_e and T_e over this radial range for these shots. Near $\rho = 0$, the average temperatures were $T_e \sim 45$ eV for the Ohmic shots and ∼130 eV for the ICRH heated shot, with separatrix densities in the range $n_e \sim (3.5$–$9.5) \times 10^{13}$ cm^{-3}. Although this table is written in terms of the distance from the separatrix, it should be noted that the separatrix location is uncertain to about 0.3 cm in C-Mod.

4. Evaluation of turbulence velocities

This section describes the evaluation of poloidally averaged turbulence velocities derived from the analysis methods of section 2 as applied to the GPI database of section 3. Section 4.1 describes the time-averaged radial and poloidal velocities, section 4.2 describes the distribution of these velocities, section 4.3 describes the frequency spectra of these velocities derived from the time-dependent analysis and section 4.4 describes the radial profile of these frequency spectra. Then section 4.5 describes the cross-correlations among radial and poloidal velocities and GPI signal level fluctuations, section 4.6 compares the poloidal velocity spectra with magnetic fluctuation spectra, and finally section 4.7 describes some results on the velocity analysis during transient events such as an L–H transition. Thus section 4.1 describes the time-averaged 'mean flows' and sections 4.3– 4.7 describe the characterization of time-dependent 'zonal flows' in these plasmas.

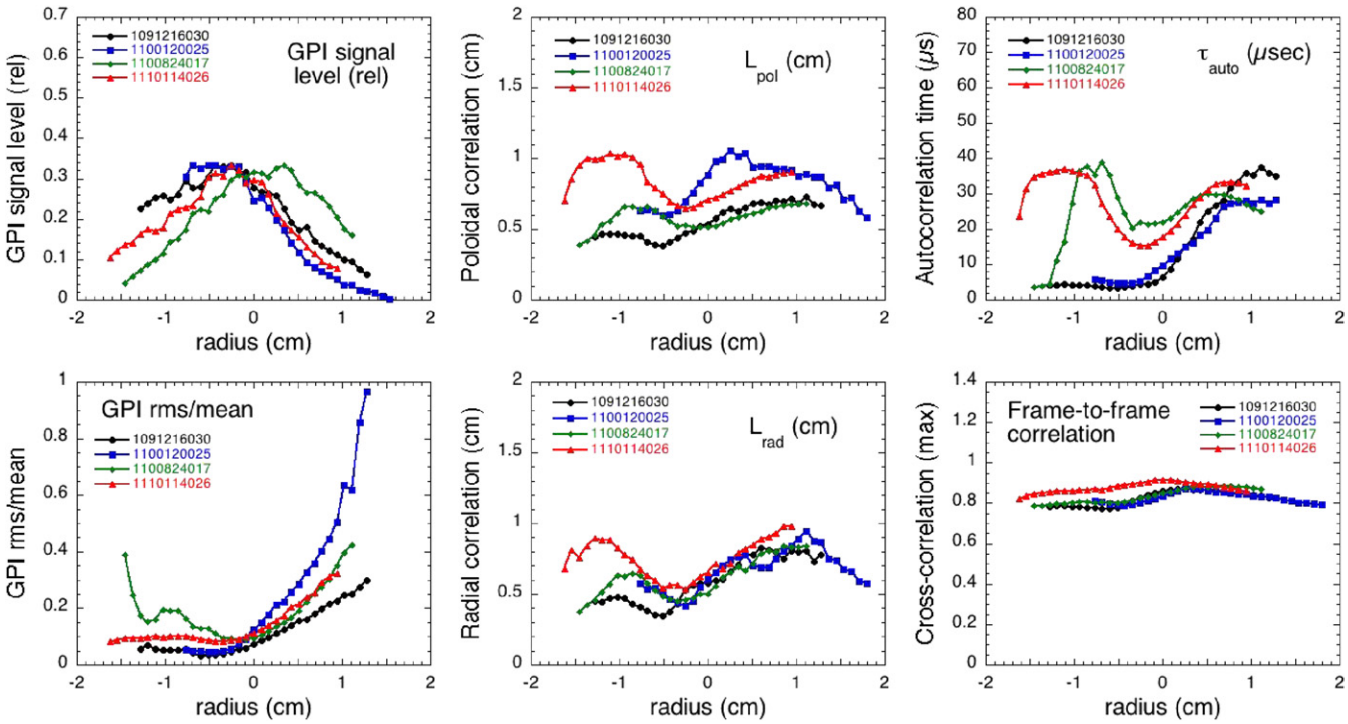

Figure 5. Typical radial profiles of turbulence characteristics for four sample shots in this database, averaged over the poloidal analysis region shown in figure 2. At the top left are the relative GPI signal profiles, at the bottom left are the relative GPI fluctuation levels, in the middle are the poloidal and radial correlation lengths, at the top right are the autocorrelation times, and at the bottom right are the maximum cross-correlation coefficients from the frame-to-frame velocity analysis.

Table 2. Typical edge and SOL densities and temperatures from Thomson scattering.

Parameter ρ (cm)	$n/10^{20}$ cm^{-3} -0.5 ± 0.3	T_e (eV) -0.5 ± 0.3	$n/10^{20}$ cm^{-3} 0 ± 0.3	T_e (eV) 0 ± 0.3	$n/10^{20}$ cm^{-3} 0.5 ± 0.3	T_e (eV) 0.5 ± 0.3
1091216028 1091216029 1091216030	0.84 ± 0.15	90 ± 26	—	—	—	—
1100120025 1100120026 1100120027	0.42 ± 0.11	104 ± 54	0.35 ± 0.08	45 ± 23	0.44 ± 0.04	21 ± 10
1100824017 1100824019 1100824024	1.2 ± 0.1	84 ± 30	$0.96 \pm .22$	46 ± 16	0.94 ± 0.18	28 ± 11
1110114023 1110114026 1110114027 1110114032	0.47 ± 0.10	340 ± 160	0.42 ± 0.13	$132 + 103$	0.35 ± 0.13	36 ± 32

4.1. Time-averaged turbulence velocities

Before discussing the time-dependent results derived from the cross-correlation analysis method of section 2.4, we first present an overview of the time-averaged radial and poloidal velocities found by averaging the time-dependent analyses over a 20 ms analysis window. These results are compared with time-averaged velocities found previously in C-Mod using other methods in section 5.3.

The top part of figure 6 shows the radial profiles of the time-averaged poloidal and radial turbulence velocities as a function of radius for the same four sample shots of figure 5. The time-averaged poloidal velocity is typically $\langle V_{pol}(t)\rangle \leqslant 1\,\mathrm{km\,s^{-1}}$ in the negative (ion diamagnetic and grad-B drift) direction, but the magnitudes and profile shapes of V_{pol} vary significantly from shot to shot. The time-averaged radial velocity is typically outward for $\rho \geqslant -0.5$ cm at $\langle V_{rad}(t)\rangle \sim 0.2\,\mathrm{km\,s^{-1}}$, but slightly inward farther into the plasma. The middle of figure 6 shows the RMS fluctuation levels of these velocities, to be discussed in section 4.2.

The bottom of figure 6 shows the radial profiles of the time-averaged poloidal velocity for all 30 shots in the database. The error bars on the points in figure 6 are the RMS variations among these velocities over the averaging time interval of 20 ms. The average poloidal velocity is always in the ion diamagnetic drift direction, but there is a considerable variation over the range of this database, as illustrated at the top of

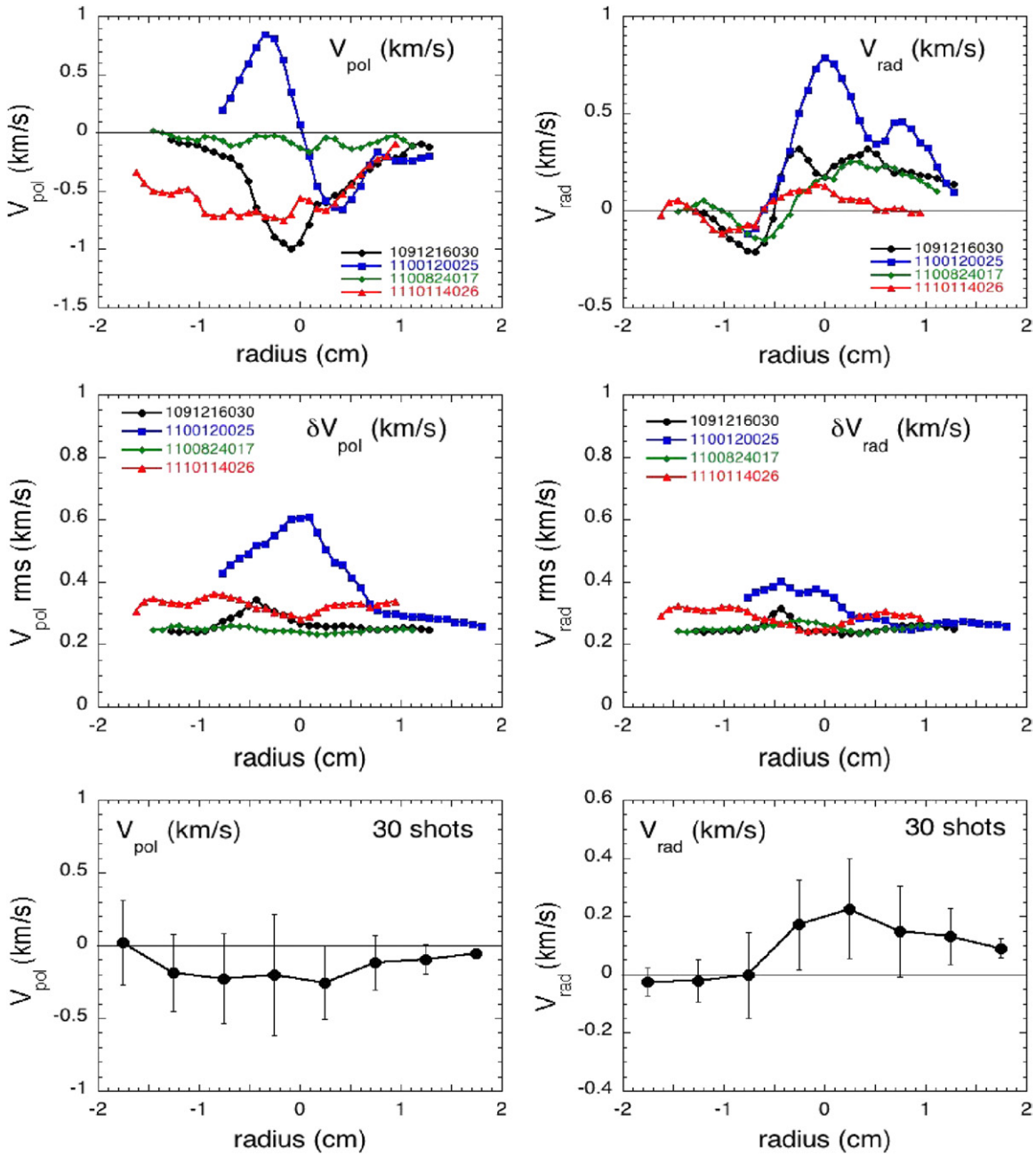

Figure 6. Radial profiles of the poloidally averaged and time-averaged V_{pol} and V_{rad} for four sample shots (top), the RMS fluctuation levels in these velocities (middle), and average of these velocities for the 30 shot database (bottom). There is a fairly wide range of profile shapes for V_{pol} within this radial range, but on average the poloidal velocity is ~0.2 km s^{-1} in the ion diamagnetic direction in the SOL. There is a fairly consistent outward V_{rad} in the SOL of ~0.2 km s^{-1}, with a slight reversal to an inward V_{rad} inside the separatrix.

figure 6. The cause of these shot-to-shot variations in the radial profiles of the time-averaged poloidal velocity is not understood at present. The time-averaged radial velocity is always outward in the SOL but inward (although small) for $\rho < 1$ cm. The relationship of this radial velocity to radial transport depends on the correlation with density fluctuations, as discussed in section 5.5.

Figure 7 shows the time-averaged poloidal and radial velocities at $\rho = 0.5$ cm in the SOL for the same database as for the correlation lengths in figure 4. The error bars on the points in figure 7 are the RMS variations of velocities over the averaging time interval of 20 ms. There is little or no dependence of these time-averaged velocities on the plasma current I_p or the plasma stored energy W, as was also the case for the turbulence quantities in figure 4. There is a slight decrease in the poloidal velocity with increasing line-averaged density or with Greenwald density in this range $n_G = 0.10$–0.35.

4.2. Distribution of turbulence velocities

A general result of these analyses is that there is a significant fluctuation level in the time-dependent poloidally averaged turbulence velocities within the GPI field of view. This was already seen in the sample velocity signals versus time in

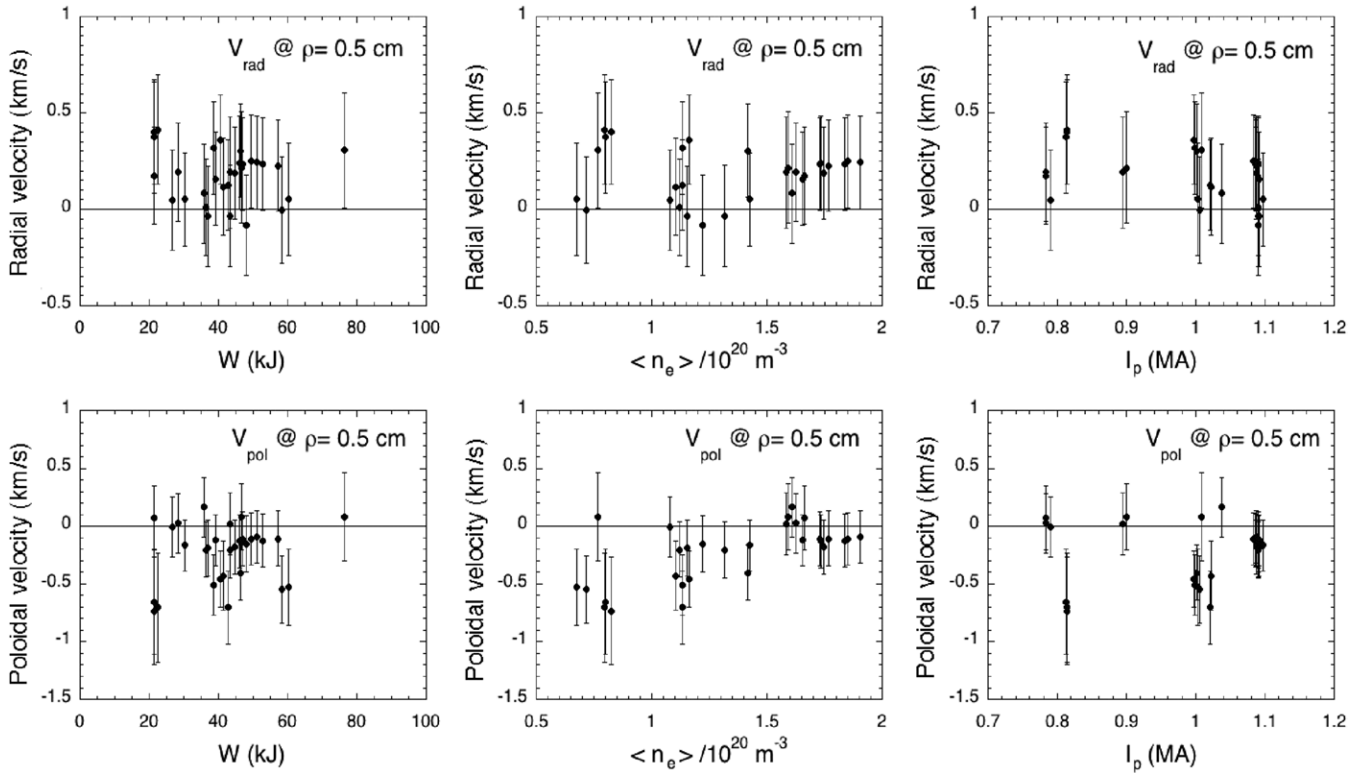

Figure 7. Poloidal and radial velocities at $\rho = 0.5$ cm for the 30 shots in this database as a function of three global plasma parameters, W (stored energy), $\langle n \rangle$ (line-averaged density) and I_p (plasma current). The RMS deviations from these average velocities are shown by the error bars. There is no clear variation in either the mean or RMS velocities with these parameters in this database (at this radius).

figure 3, and in the RMS velocity fluctuations in figure 6, which had a fluctuating component of $\delta V_{pol} \sim 0.3\,m\,s^{-1}$, i.e. comparable to the time-averaged velocities. This was further illustrated in figure 7, which shows the velocities calculated at $\rho \sim 0.5$ cm for all shots in the database, including the RMS fluctuations as error bars on the average velocities. Furthermore, figure 7 shows that there were no strong trends in the RMS radial or poloidal velocities as a function of stored energy, plasma current or line-averaged density in this database (at this location). In all cases the velocity fluctuations are comparable in magnitude to the mean velocities.

Figure 8 shows an example of the probability distributions of the radial and poloidal velocities for three different radii ($\rho = 0$ cm and $\rho = \pm 0.8$ cm) for one case (1091216030), averaged over 20 ms. The velocity distributions are all quite broad, with a roughly Gaussian distribution with an RMS in velocity typically $\delta V \sim 0.3\,km\,s^{-1}$. The velocity distributions in all other cases are similarly broad. The bottom of figure 8 shows the distributions of V_{pol} jointly with V_{rad} for the same shot, where each point corresponds to the velocity evaluated for a single time frame (averaged over $\pm 12.5\,\mu s$) for this shot. There is a small linear correlation between the V_{pol} and V_{rad} for the $\rho \sim 0.0$ cm cm cases, but not for the $\rho \sim \pm 0.8$ cm cases. The cross-correlation between radial and poloidal velocity fluctuations is further discussed in section 4.5.

4.3. Frequency spectra of turbulence velocity

To look for organized zonal flows within these fluctuations in turbulence velocity, it is very helpful to examine the frequency spectra of these velocity fluctuations. Figure 9 shows two examples of the frequency spectra of V_{rad} (left) and V_{pol} (right) as a function of time over 20 ms at $\rho = -0.5$ cm for shot 1100120025 (top) and 1110114026 (bottom). These time-resolved spectra are evaluated using an FFT averaged over 800 frames (~2 ms) at each time point, and the spectra are uncorrected for the frequency response of the velocity analysis, i.e. the sensitivity to velocity fluctuations in this plot falls by about $1/e$ at ~30 kHz (see the '25 μs' curve of figure 3).

The case at the top (110110025) shows no apparent coherent features in the spectrum of either δV_{rad} or δV_{pol} in the range ~1–30 kHz, although there are intermittent bursts of duration ~1 ms with varying frequency in the range ~1–20 kHz. Most of the shots in table 1 have spectra which look qualitatively similar to those at the top of figure 9. However, the case at the bottom (1110114026) does show a clear coherent feature at ~6–7 kHz in the δV_{pol} spectrum for $\rho = -0.4$ cm. This coherent feature in δV_{pol} persists over at least 70 ms, and is also seen at other radii (see next section). There is little or no coherent feature in V_{rad} at this frequency.

Figure 10 shows the δV_{pol} frequency spectra for the four sample shots used in figure 6 for three radial locations, $\rho = -0.8$ cm, $\rho = 0.0$ cm and $\rho = 0.8$ cm. The top plots show the two shots of figure 9, and the bottom plots show the two other sample shots, all of which are averaged over 20 ms (note the varying vertical scales). The coherent mode at ~6–7 kHz in shot 1110114026 of figure 9 can be seen at all three radii in figure 10, although with a lower amplitude at $\rho = 0.8$ cm. The more broadband, intermittent frequency spectrum seen in

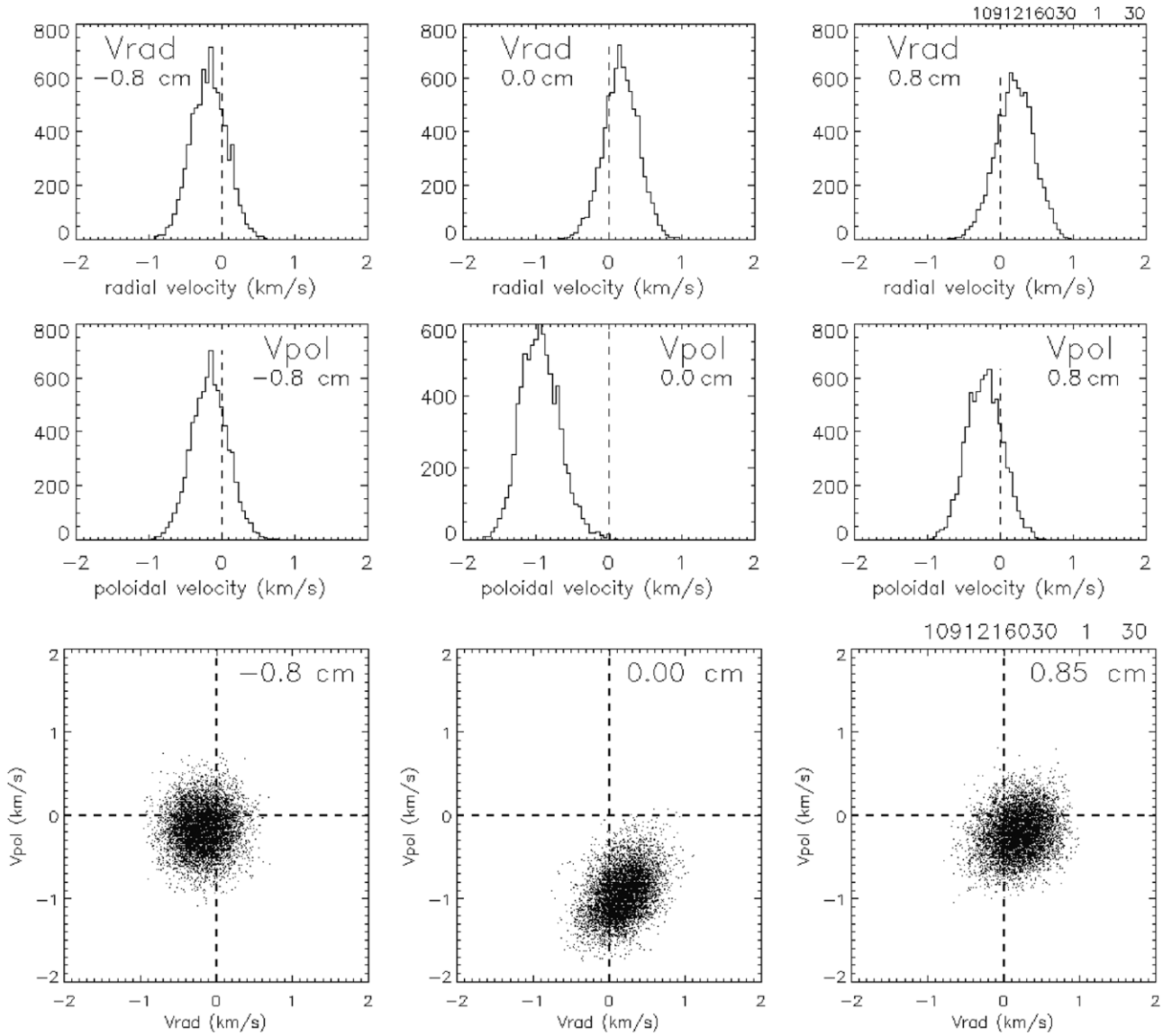

Figure 8. The top two panels show the distributions of V_{rad} and V_{pol} for three different radial locations in one shot (in 10912160330), averaged over 20 ms. The velocities have a large spread around their mean values in all cases. The bottom panel shows the joint distributions of V_{rad} versus V_{pol} for each time point for the cases above for the three different radial locations in 10912116030. There is a slight correlation between V_{rad} and V_{pol} at $\rho = 0$ cm.

shot 1100120025 in figure 9 also seems to have a residual time-averaged spectral structure at $\rho = 0.0$ cm in figure 10, but with different and lower amplitude spectra at $\rho = \pm 0.8$ cm. One of the other two typical shots shown at the bottom of figure 10 (1091216030) has a similar but smaller broadband intermittent structure, but the other shot (1100824017) seems to have no significant time-averaged spectral features.

The magnitude of this coherent velocity oscillation for 1110114026 near ~6–7 kHz between $\rho = -0.8$ cm and $\rho = -0.0$ cm is ~0.2 km s^{-1}, as determined from comparing the peak in this spectrum with a forced oscillation of the raw image data at this frequency. The full end-to-end amplitude of the poloidal motion corresponding to this oscillation is ~1 cm. However, this poloidal motion cannot easily be seen in the movies of this shot [34] since the turbulence correlation times (~10–30 μs) are much shorter than the period of this oscillation (~150 μs).

4.4. Radial profiles of poloidal velocity spectrum

Radial profiles of the poloidal velocity fluctuation spectra are illustrated in figure 11 for the top two shots of figure 10, each for three different times. These spectra are again calculated over 800 frames centered at the times shown in each panel. For the case at the top (1100120025), the velocity fluctuations have a band-like spectra extending over radius in the region $\rho = -0.5$ cm to +0.5 cm; however, this structure changes slowly in time over 20 ms, which leads to the broad and intermittent spectra shown in figures 9 and 10. In the lower case (1110114026), the velocity fluctuations have a dominant peak near ~6–7 kHz everywhere in the region $\rho = -1.0$ cm to +0.5 cm for all times, which corresponds to the peak in the spectrum of figure 10. Movies of the time evolution of these spectra can be found in [34].

There were only two other shots in this database which had a coherent δV_{pol} peak at ~6–7 kHz, i.e. 1110114027 and

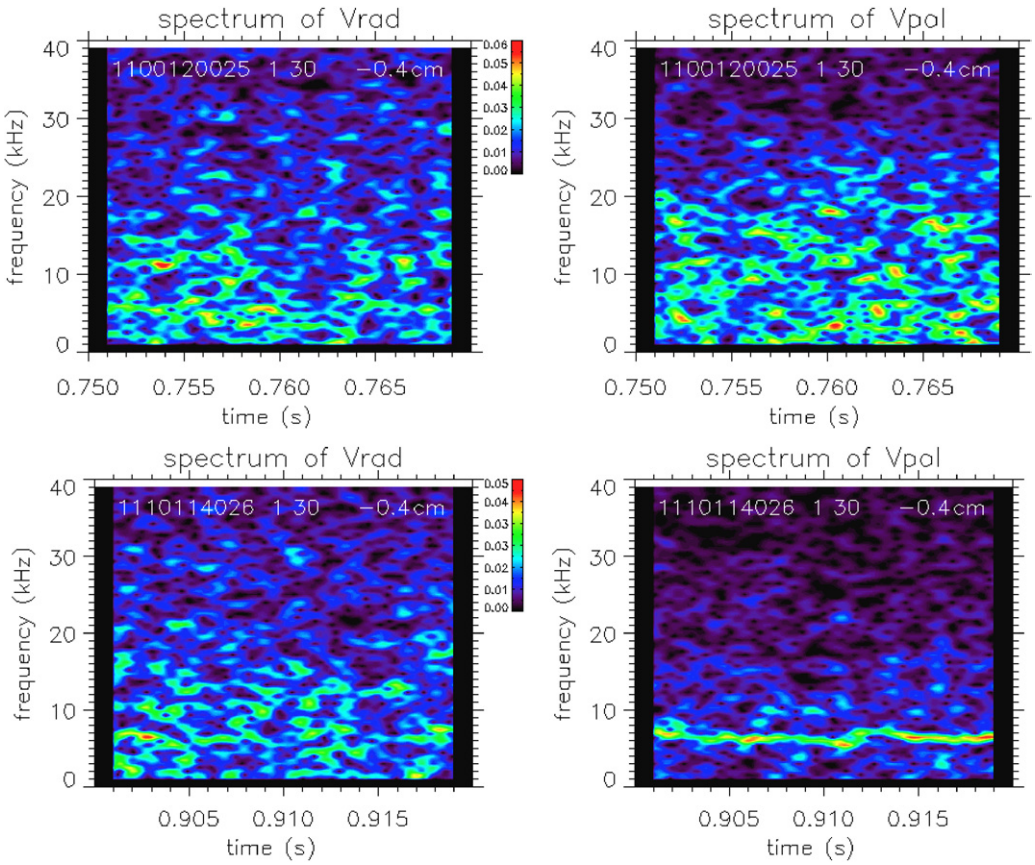

Figure 9. Examples of frequency spectra of the velocity fluctuations $\delta V_{\rm rad}$ and $\delta V_{\rm pol}$ for $\rho = -0.5$ cm for two sample shots (1100120025 and 1110114026). The amplitude spectrum of $\delta V_{\rm pol}$ is broadband and intermittent for shot 1100120025, but the amplitude spectrum has a near-coherent component at 6–7 kHz for shot 1110114026. The $\delta V_{\rm rad}$ do not have a clear coherent feature in either case.

1110114032. Many other shots had broadband intermittent spectra like 11001120025 (e.g. 1100120026, 1100120027, 1091216028, 1091216029 and 10912116030). Surprisingly, shot 1110114023 did not have a coherent mode, even though it was superficially similar to 11004026. However, the ICRH resonance location in the coherent $V_{\rm pol}$ cases 1110114026, 027 and 032 was located on axis or on the low-field side of the axis, whereas the resonance for 1110114023 was located on the high-field side.

In order to help clarify the radial extent of these poloidally averaged poloidal velocity fluctuations, the radial width of the zero-time-delay normalized cross-correlation function of $\langle \delta V_{\rm pol} \delta V_{\rm pol} \rangle$ was evaluated for all shots in table 1, as shown in figure 12. To find this width, the location of maximum cross-correlation of $\delta V_{\rm pol}$ with itself over a radial separation of 0.35 cm was first found for radii inside the separatrix; then the FWHM of the radial cross-correlation function around this maximum was determined. The results in figure 12 are plotted as a function of the line-averaged density for these shots, and these widths are also shown at the right of table 1. There is a clear trend toward a decrease in this width with increasing $\langle n_{\rm e} \rangle$, as shown by the linear fit (for the first 30 shots of table 1). But by far the largest width (∼2.1 cm) was for the one shot in which an L–H transition occurred just after the time analyzed (1110114032). The two sample shots with largest $\delta V_{\rm pol}$ spectral features in figure 10 (i.e. 1110114026 and 1100120025) were located within the group of points near the lowest density and highest width (∼0.88 and 0.78 cm, respectively), while the sample shot with the smallest spectral features in figure 10 (i.e. 1100824017) was located at the highest density and lowest width (∼0.15 cm), and the other sample shot (1091216030) was somewhere in between in density and width (0.5 cm). Radial profiles of these cross-correlations of $\delta V_{\rm pol}$ for the sample cases are shown in the next section.

Note that the dependence of the radial cross-correlation widths of $\delta V_{\rm pol}$ with density shown in figure 12 does *not* imply that the magnitude of $\delta V_{\rm pol}$ varies this way with density. In fact it does not, as shown for the four sample cases in the middle of figure 6, and for the larger database for $\rho = 0.5$ cm in figure 7. At the location of the maximum cross-correlation $\delta V_{\rm pol}$ neither the poloidal flow fluctuations $\delta V_{\rm pol}$ nor the amplitudes of $V_{\rm pol}$ are correlated with density in this same database. Note that the variation with density in figure 12 might be related to changes in the radial correlation lengths of the underlying turbulence with density, as discussed in section 5.4.

4.5. Correlations of radial and poloidal velocity

The radial profiles of various cross-correlations of the fluctuations in the poloidally averaged $\delta V_{\rm pol}$ and $\delta V_{\rm rad}$ with each other and with the fluctuations in the GPI signal level itself are shown in figure 13 for the four sample shots used in figures 6 and 10. All these cross-correlations are averaged

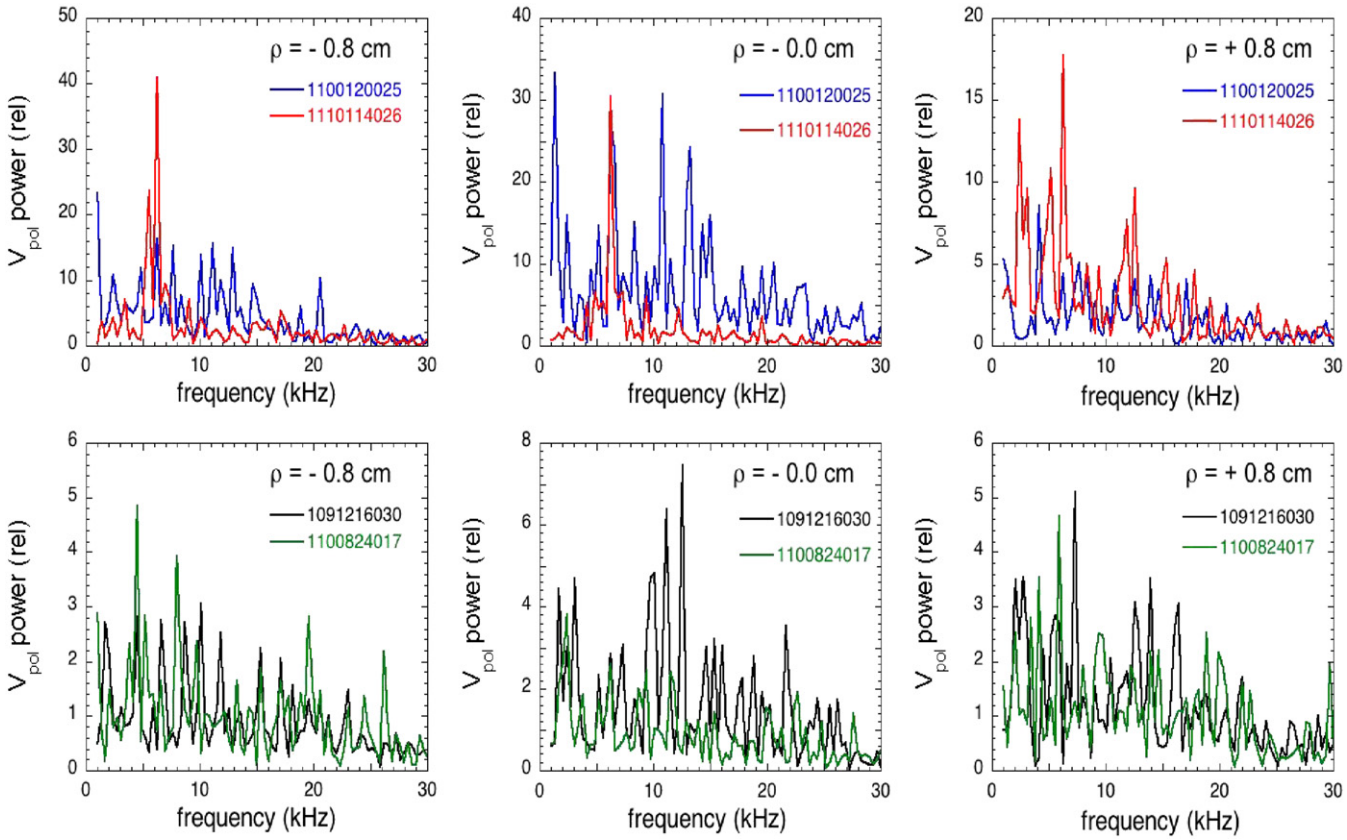

Figure 10. Frequency spectra of poloidally averaged $\delta V_{\rm pol}$ for the four sample shots of figure 6 for three different radii $\rho = -0.8$ cm, 0.0 cm and +0.8 cm. These power spectra are averaged over 20 ms for each case. The coherent peak in 1110114026 appears at all radii. Note the varying vertical scales for each plot.

over the ∼7800 time samples in the 20 ms analysis period for each shot, so the random cross-correlation level is very small in all cases (∼1%).

Sample zero-time delay radial cross-correlations of the poloidal velocity fluctuations $\delta V_{\rm pol}$ with themselves, with a radial separation of 0.35 cm, are shown at the upper left of figure 13 (similar to the analysis used for figure 12). For the shot with the 6–7 kHz coherent feature (1110114026) these $\delta V_{\rm pol}$ cross-correlations are $\geqslant$0.5 over the radial range ±1 cm. The following shot with a similar coherent feature (1110114027) was similar, and the pre L–H transition shot (1110114032) has an even higher cross-correlation of $\geqslant$0.75 over this same spatial range (not shown). Thus the radial structure of the velocity fluctuations extends over at least ±1 cm around the separatrix in the cases with a $\delta V_{\rm pol}$ coherent feature. For the less coherent cases such as 110120025 and 1091216030 in figure 13, the $\delta V_{\rm pol}$ cross-correlation is highest near the separatrix, but falls off inside and/or outside this radius.

The cross-correlation between the poloidally averaged $\delta V_{\rm pol}$ and $\delta V_{\rm rad}$ at zero time delay and zero radial separation is shown at the upper right of figure 13. There is a significant cross-correlation for at least three of these four sample shots, and also for the L–H transition shot (not shown). These cross-correlations can be related to the Reynolds stress, as discussed in section 5.5.

The zero-time delay cross-correlations of the GPI signal intensity fluctuations $\delta I_{\rm GPI}$ (also averaged over the poloidal analysis region) with $\delta V_{\rm pol}$ or $\delta V_{\rm rad}$ are shown at the bottom of figure 13. There appears to be a significant negative correlation of $\delta V_{\rm pol}$ with $\delta I_{\rm GPI}$ just inside the separatrix for 1110114026, which is similar to the relationship between these two quantities seen in NSTX [17], i.e. the fluctuation level decreased when the $V_{\rm pol}$ was in the positive (electron diamagnetic drift) direction. For the other sample shots there is only a low correlation ($\leqslant$0.2) of $\delta I_{\rm GPI}$ with $\delta V_{\rm pol}$, or for $\delta I_{\rm GPI}$ with $\delta V_{\rm rad}$. The possible relationship between these correlations and turbulent transport is discussed in section 5.5.

4.6. Correlation with magnetic fluctuations

Figure 14 shows part of the $\delta V_{\rm pol}$ power spectra versus frequency for $\rho = 0$ cm for two shots (1100120025 and 1110114026), averaged 20 ms, overlaid with the MHD power spectrum of poloidal magnetic field fluctuations from an edge magnetic coil (BP1T_GHK) for the same shots. The peaks in the spectrum of $\delta V_{\rm pol}$ for shot 1100120025 (right) do not coincide with those in the magnetic spectrum. However, for the coherent mode in the $\delta V_{\rm pol}$ spectrum of 1110114026 at ∼6–7 kHz does coincide with an MHD peak at this frequency. A similar frequency match occurred $\delta V_{\rm pol}$ and MHD for the similar shot 1110114027, and also for the pre-L–H transition case 1110114032, during which the frequency-resolved coherence coefficient between $\delta V_{\rm pol}$ and the magnetic signals was $\geqslant$90% at ∼6 kHz. However, an apparently similar

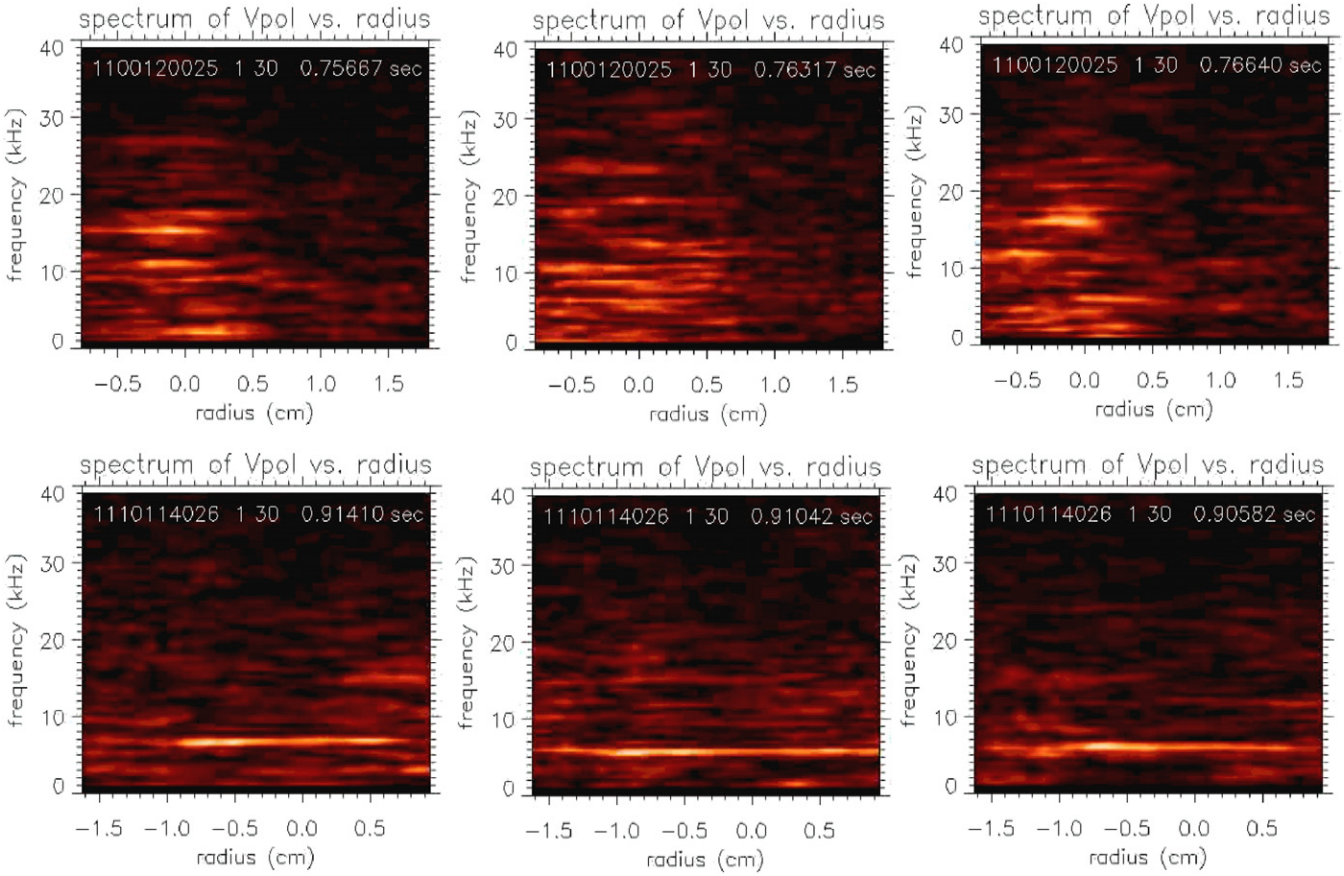

Figure 11. Radial profiles of frequency spectra of $\delta V_{\rm pol}$ for three different times for the two sample shots of figures 9 and 10. For the top case (1100120025) the poloidal field fluctuations in the range ∼1–20 kHz are mainly localized within $\rho = \pm 0.5$ cm, but for the bottom case the near-coherent oscillation at 6–7 kHz is spread over at least $\rho = \pm 1$ cm.

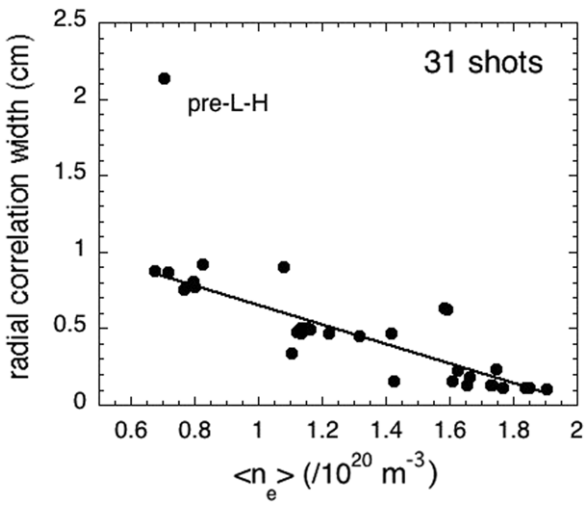

Figure 12. Radial width (FWHM) of the normalized cross-correlation of $\langle \delta V_{\rm pol} \delta V_{\rm pol} \rangle$ for all the shots from table 1. This width decreases with line-averaged density for 30 shots, as fit by the line shown, but is much larger for the one 'pre-L–H' shot with a subsequent L–H transition (1110114032). All these cross-correlations are evaluated inside the separatrix.

shot 1110114023 had neither a coherent peak in $V_{\rm pol}$ nor an MHD peak near 6–7 kHz. Thus for all shots with a coherent $\delta V_{\rm pol}$ feature there is a correlation between the edge poloidal velocity and magnetic fluctuations.

Also shown in figure 14 are the spectra of the GPI signal fluctuations $\delta I_{\rm GPI}$ at $\rho = 0$ cm for the same two shots, also averaged over poloidal angle. There is a peak in the $\delta I_{\rm GPI}$ spectrum at the same 6–7 kHz frequency as in $\delta V_{\rm pol}$ and MHD spectra for shot 1110114026, suggesting that the GPI signal fluctuations are modulated with the poloidal flow fluctuations in this case. In fact, the radial profile of the zero-time cross-correlation of $\delta V_{\rm pol}$ and $\delta I_{\rm GPI}$ was shown at the lower left of figure 13 to be as high as 0.4 just inside $\rho = 0$ cm. A significantly lower correlation between these two fluctuating quantities was seen in the other sample shot 1100120025. Preliminary analysis of the coherent MHD signal at 6 kHz suggests it is dominated by $n = 0$. Further analysis of the phase relations between these three fluctuating quantities will be deferred to a future publication.

4.7. Transient events

For all data discussed so far the turbulence velocities have been analyzed during stationary plasmas. However, for shot 1110114032 there was an L–H transition shortly after the analysis time of 0.90–0.92 s. Figure 15 shows the $\delta V_{\rm pol}$ spectrum versus time for this shot when there was an L–H transition at 0.923 s, and subsequent ELMs at 0.931 s, 0.938 s and 0.948 s.

At the left of figure 15 is the spectrum of $\delta V_{\rm pol}$ versus time at $\rho = -0.4$ cm, which shows a sudden decrease in the

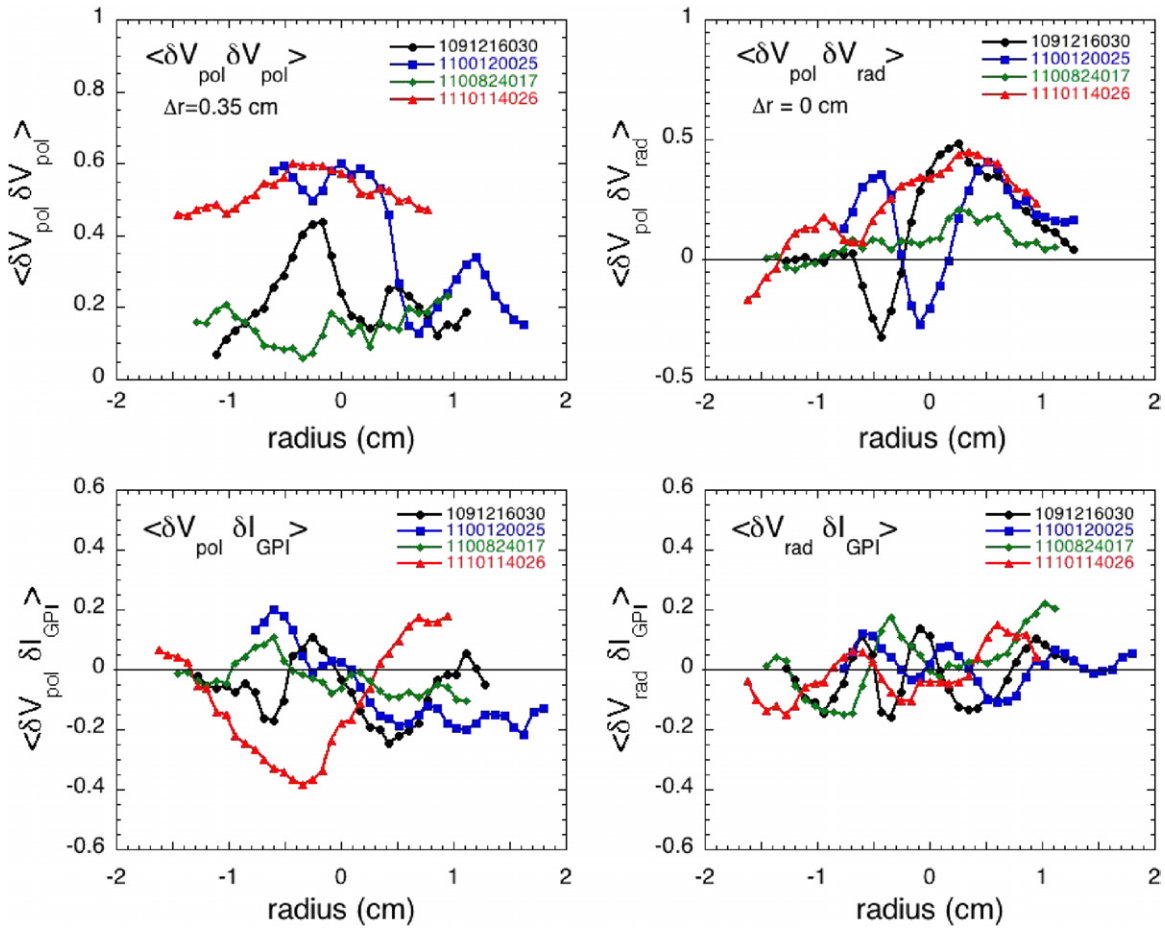

Figure 13. Normalized zero-time delay cross-correlation coefficients of poloidal and radial velocity fluctuations with each other and with the GPI signal level fluctuations $\delta I_{\rm GPI}$ (averaged over the poloidal viewing region). At the upper left is $\langle \delta V_{\rm pol}(r-\Delta/2)\delta V_{\rm pol}(r+\Delta/2)\rangle$, where $\Delta = 0.35$ cm. At the upper right is $\langle \delta V_{\rm pol}(r)\delta V_{\rm rad}(r)\rangle$, which is related to the Reynolds stress. At the bottom are $\langle \delta V_{\rm pol}\delta I_{\rm GPI}\rangle$ and $\langle \delta V_{\rm rad}\delta I_{\rm GPI}\rangle$, which are correlations of the poloidal velocity fluctuations with the GPI signal fluctuations.

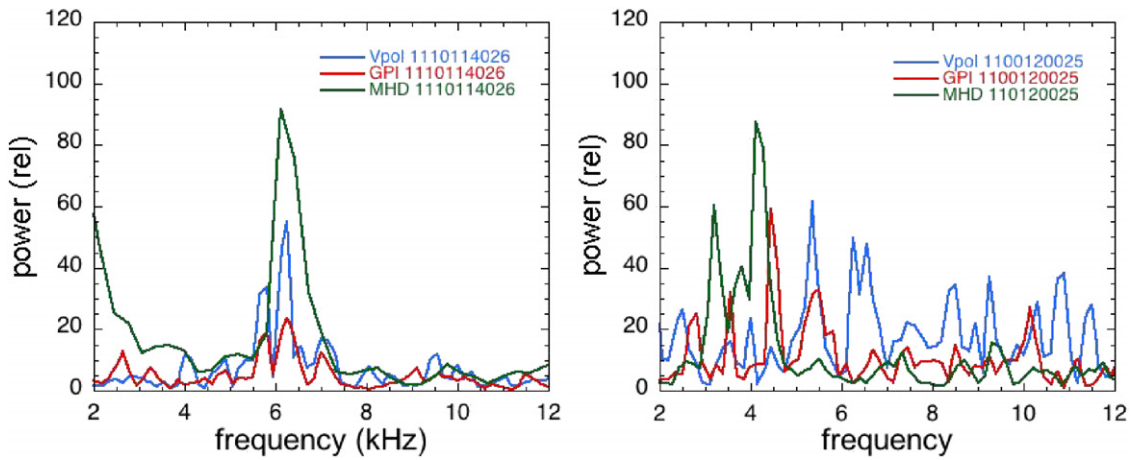

Figure 14. Comparison of the frequency spectra of $\delta V_{\rm pol}$ at $\rho = 0$ cm for the two shots of figures 9 and 11 (blue) with the MHD spectrum from a B-dot coil at the wall (green), and the GPI signal fluctuation spectrum (red), all averaged over 20 ms. There is a coincidence between the $\delta V_{\rm pol}$ oscillation at 6–7 kHz and the MHD and GPI signals in the case at the left, but no correlation of these features in the case at the right.

coherent feature at ~6 kHz at the time of the L–H transition. At the right of figure 15 is the time dependence of the amplitude of this coherent feature in $\delta V_{\rm pol}$ integrated over 5–7 kHz for three different radii: $\rho = 0.0$ cm and $\rho = \pm 0.4$ cm. For each of these radii the $\delta V_{\rm pol}$ amplitude decreases by a factor of ×5–10 within ~10 ms after the transition, and the amplitude of the MHD mode at this frequency also decreases similarly at this time (not shown). The slow ~0.5 kHz time variations in coherent ~6 kHz oscillations in $\delta V_{\rm pol}$ before the transition are also highly correlated among these channels, as discussed

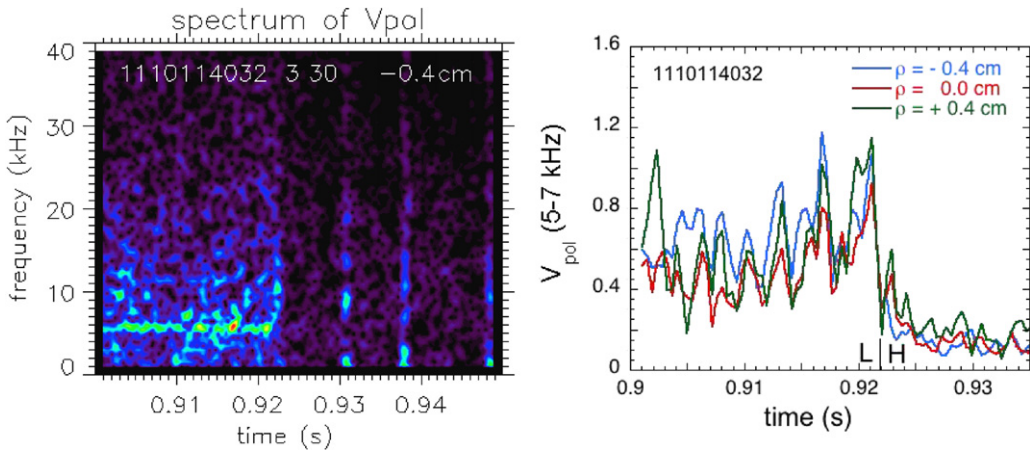

Figure 15. At the left is the $\delta V_{\rm pol}$ spectrum versus time of shot 1110114032 at $\rho = -0.4$ cm, showing a coherent oscillation at ~6 kHz which decreases in amplitude at the L–H transition at 0.922–0.923 s. At the right is the $\delta V_{\rm pol}$ magnitude versus time within the frequency range 5–7 kHz for three radii for this shot, showing that the amplitude of the coherent oscillation decreases at the same time across over these radii, and that the ~0.5 kHz fluctuations preceding the L–H transition are common to all three radii.

briefly in section 5.6. The $\delta V_{\rm rad}$ signals show no coherent oscillation and no significant changes at the L–H transition.

The analysis of the radial width of the $\langle \delta V_{\rm pol} \delta V_{\rm pol} \rangle$ cross-correlation for the 'pre-L–H' shot in figure 12 was done by averaging over a 20 ms time period ending 3 ms before the L–H transition. A more detailed time-dependent analysis showed that there were no significant time variations of this correlation width during the 23 ms before the transition, and only a small decrease afterward; thus the main transient observed with the L–H transition in this case was in the amplitude of $\delta V_{\rm pol}$ and not its correlation width. These poloidal velocity analyses average over a few turbulence correlation times and over the poloidal range of the GPI view, so the detailed transient structure in the last 50 μs before the transition was not resolved.

Transient changes in the turbulence velocities were also seen during the ELMs of figure 15. The GPI signal level increases for ~1 ms in the SOL at the ELM crashes, similarly to NSTX [41]. The $\delta V_{\rm pol}$ has several large oscillations before and during the crash, and there was a transient increase in $\delta V_{\rm rad}$ at the crash. All signals return to their pre-ELM state about 1 ms after the crash. One other example of transient behavior of turbulence velocities was shown for shot 1110114026 in figure 9, which had a sawtooth crash at 0.0911–0.912 s. In this case there was a slight increase in the coherent oscillation frequency of $\delta V_{\rm pol}$ coincident with the sawtooth crash, with a return to the original frequency after ~3 ms.

5. Discussion

This section contains a summary of the experimental results in section 5.1, a discussion of their uncertainties and limitations in section 5.2, a comparison with other time-averaged velocity measurements on C-Mod in section 5.3, a comparison with the theory of zonal flows in section 5.4, a discussion of velocity cross-correlations in section 5.5, a discussion of the relationship to other experimental results in section 5.6 and a conclusion and some further directions in section 5.7.

5.1. Summary of experimental results

The new results of this paper concern time-dependent measurements of the poloidal and radial velocity of the edge turbulence in C-Mod, evaluated using the cross-correlation analysis method described in section 2.4, as illustrated in figures 2 and 3. These velocities were averaged over the poloidal range of the GPI diagnostic to search for large-scale zonal flows. Limitations of this velocity algorithm are discussed in section 5.2.

The edge turbulence characteristics for the database of table 1 were described in section 3.2 and shown in figures 4 and 5, and are consistent with those described previously for Alcator C-Mod [27–31]. Figure 4 shows that the poloidal and radial correlation lengths are almost independent of the plasma current (at fixed q_{95}), density and stored energy. Figure 5 shows that the radial correlation lengths are fairly independent of minor radius for four sample shots, and that the relative GPI fluctuation levels consistently decrease from the SOL to inside the separatrix, as usual for edge turbulence.

The time-averaged radial and poloidal velocities were described in section 4.1 and figures 6 and 7. There was a considerable shot-to-shot variation in the poloidal velocity profile among these shots, but the average poloidal velocity was in the ion diamagnetic drift (and grad-B drift) direction within ±2 cm of the separatrix. The radial velocity was consistently outward in the SOL, but was slightly negative (i.e. inward) for $\rho \leqslant -1$ cm. Figure 7 showed that there was no systematic variation of these time-averaged velocities with plasma current, density or stored energy, at least at this radius of $\rho = -0.5$ cm.

Radial profiles of the RMS fluctuation levels in the poloidally averaged poloidal and radial velocity were also shown in figure 6 for the four sample cases. These fluctuations were typically ~0.2–0.4 km s^{-1}, which was comparable to the typical mean or time-averaged velocities. The distribution functions of velocity were typically broad, as illustrated in figure 8, and there was a slight correlation between radial and poloidal velocity also shown in figure 8. In all cases both

the radial and poloidal velocities had a significant fluctuating component.

The frequency spectra of the poloidal and radial velocity fluctuations for two of the sample shots were shown in figure 9. For one case (1100120025) there were only random-looking intermittent peaks in the poloidal velocity spectrum, while for the other case (1110114026) there was a nearly coherent oscillation in the poloidal flow at ~6–7 kHz, which looked (at least superficially) like a GAM, as discussed in section 5.4. There was no clear coherent peak in the radial velocity spectra, so further analysis was done only for the poloidal velocity spectra. Examples of these spectra for the four typical shots were shown in figure 10 for three different radii, and radial profiles of these spectra at three times for two shots are shown in figure 11. The coherent feature at 6–7 kHz of 1110114026 extends over at least ±1 cm around the separatrix, while the more complex spectrum of 1100120025 was localized within about ±0.5 cm of the separatrix.

A measure of the radial correlation of the poloidal flow fluctuations was shown in figure 12, which plotted the width of the normalized cross-correlation $\langle \delta V_{\rm pol} \delta V_{\rm pol} \rangle$. This correlation showed a surprisingly clear dependence on the line-averaged density, with the highest cross-correlation width at the lowest densities. This suggests that density is a significant variable in determining the poloidal flow profile in this database, perhaps associated with collisional damping, as discussed in section 5.4.

Radial profiles of the cross-correlations among poloidal and radial velocity fluctuations and the GPI signal level fluctuations were shown in figure 13 for the four sample cases. The zero-time delay cross-correlation of $\langle \delta V_{\rm pol}(r) \delta V_{\rm rad}(r) \rangle$ was significant, and will be related to the Reynolds stress in section 5.5. The zero-time delay cross-correlations between $\delta V_{\rm pol}$ and $\delta I_{\rm GPI}$ were large in only one case, and those between $\delta V_{\rm rad}$ and $\delta I_{\rm GPI}$ were small in all cases, as discussed in section 5.6.

The frequency spectra of $\delta V_{\rm pol}$ were compared with the magnetic fluctuation spectra in figure 14, and a coincidence between the coherent $\delta V_{\rm pol}$ oscillation at 6–7 kHz and a large peak in MHD spectrum was found. The coherent $\delta V_{\rm pol}$ decreased significantly at the L–H transition, as illustrated by another shot in figure 15, and there were also transient variations of $\delta V_{\rm pol}$ during ELMs and sawtooth crashes.

5.2. *Limitations and uncertainties in experimental results*

A fundamental limitation of these results is that the velocity measured in this analysis is that of the small-scale turbulence seen in the GPI images, and not that of the fluid (or $E \times B$) velocity of the plasma itself. Thus we need to assume that the turbulence motion in these images is dominated by the local $E \times B$ flow in order to interpret the poloidal oscillations in velocity as a zonal flow, or the radial velocity as a convective transport. Although the poloidal velocity of edge turbulence has been identified with the zonal flow in previous measurements, e.g. [9, 12], there could be an additional velocity of the turbulence within the plasma rest frame. For example, it is sometimes assumed (although not proven) that edge turbulence moves poloidally at the electron diamagnetic drift speed in the plasma rest frame [1, 2]. For a typical case near the separatrix (1110114026) where $T_{\rm e} \sim 150$ eV and $L_{\rm n} \sim 3$ cm (see table 2), the time-averaged diamagnetic velocity is $V_{\rm pol} \sim 1\,{\rm km\,s^{-1}}$, which is comparable to the measured poloidal turbulence velocity. Unfortunately, the fluctuations in the diamagnetic drift speed cannot be directly evaluated or subtracted out from the measured velocity, since there is not enough information on time-dependent edge density and temperature profiles at high frequencies (~2–30 kHz).

The other major limitation of these results is that the poloidal velocities were averaged locally over only 4 cm in the poloidal direction (about five poloidal correlation lengths), so the derived velocities were not the truly global (i.e. $m = 0$) 'zonal' component of these flows. Although a similar limitation applied to the many previous measurements of zonal flow, e.g. [9–19], it would be useful to search for zonal flows using two measurements separated by much larger distance, e.g. as in [20–26]. Also left somewhat uncertain in this analysis is the sensitivity of the velocity results to the amplitude or correlation lengths of the turbulence, which might, for example, affect the interpretation of the decrease in the coherent flow feature after the L–H transition in figure 15.

There are also specific limitations to the velocity algorithm described in section 2.4. The cross-correlation analysis searches only in an 8 × 8 pixel range to find the best frame-to-frame match, so only velocities $\leqslant 2.7\,{\rm km\,s^{-1}}$ can be found with this method (see also section 5.3). These analyses also make the approximation that the poloidal direction is vertical in these images, so averaged over the ~1–2 mm variation in ρ in a given column (see figure 2). Since this is comparable to the spatial resolution of the diagnostic, and smaller than the radial correlation length of the edge turbulence, it is not a significant limitation.

5.3. *Comparison with other turbulence velocity analyses in C-Mod*

Other techniques have been used previously to evaluate the time-averaged poloidal and radial turbulence velocity in Alcator C-Mod. Radial versus poloidal velocity fields were first evaluated with a cross-correlation algorithm in [27] using 2D GPI data taken at 250 000 frames s^{-1} and averaged over 300 frames (i.e. 1.2 ms). Poloidal velocities inside the separatrix were found to be dominant ~ 0.3–$1\,{\rm km\,s^{-1}}$ in the ion diamagnetic drift direction, and radial velocities outward outside the separatrix were $\sim 0.5\,{\rm km\,s^{-1}}$, i.e. both similar to those found here (figure 6). Radial velocities of spatiotemporal structures (i.e. blobs) were subsequently evaluated using time-delayed cross-correlations within GPI images and between GPI images and a moving Langmuir probe [28]. A broad distribution of radial and poloidal structure velocities was found for $V_{\rm pol}$ within the range $\pm 1\,{\rm km\,s^{-1}}$ and for $V_{\rm rad}$ in the range $-0.5\,{\rm km\,s^{-1}}$ to $+1\,{\rm km\,s^{-1}}$, but with an average $V_{\rm rad} \sim 0.5\,{\rm km\,s^{-1}}$ outward, i.e. similar to the distributions found (figure 8).

The time-averaged radial turbulence speed from GPI camera data was recently studied using a cross-correlation

analysis for an L-mode plasma current scan in [29]. Outward radial speeds in the range $V_{rad} \sim 0.2\,km\,s^{-1}$ in the SOL were found at 0.8–1.1 kA, and reversal of the radial speed to inward propagation was found near the separatrix, both similar to the results of figure 6. These behaviors are qualitatively consistent with theoretically expected propagation characteristics of blobs (outward) and holes (inward). Recently, GPI turbulence velocities in C-Mod in different density regimes were analyzed using both cross-correlation and conditional sampling techniques [31]. In the density range at $n/n_G \leqslant 0.3$, as used in this paper, the time-averaged V_{pol} were within $\pm 1\,km\,s^{-1}$ and the time-average $V_{rad} \sim$ 0.3–0.5 $km\,s^{-1}$, similar to figure 6.

A direct comparison was made between the time-averaged velocities obtained from a blob-tracking algorithm similar to [29] with the time-averaged velocities obtained from the algorithm of section 2.4 here. The results were very close to each other in magnitude and radial profile, i.e. differing by an average of only $\sim 0.05\,km\,s^{-1}$. A direct comparison was also made between the cross-correlation and the conditional averaging algorithms of [31] and the algorithm of section 2.4. The conditional sampling velocities were also close to those obtained here where they could be compared in the SOL, but in some cases the cross-correlation algorithm of [31] produced velocities which differed from those obtained here by up to ~ 0.5–$1\,km\,s^{-1}$. This is most likely due to a different type of space and time-averaging used in the two different algorithms. This points out that the turbulence velocities obtained for these GPI images do depend somewhat on the algorithm used to extract them.

Finally, spatial and temporal Fourier analyses were made on the GPI data from the 2D array of views coupled to photodiodes [30]. These analyses yield wavenumber versus frequency spectra and time-averaged poloidal phase velocities of $\sim 2\,km\,s^{-1}$ in the ion diamagnetic drift direction, along with a $\sim 4\,km\,s^{-1}$ phase velocity in the electron diamagnetic drift direction inside the separatrix. These poloidal phase velocities are significantly higher than the poloidal velocities determined from the cross-correlation analysis in this paper. A detailed analysis of the difference between these two techniques is important, but is deferred to a future publication.

5.4. Comparisons with theories of zonal flow

The main motivation for this paper was to search for edge zonal flows in Alcator C-Mod. The result from this study is that some evidence for zonal-like flows was found, although a clear quantitative connection between experiment and theory has not been established, as discussed below.

The clearest evidence for a zonal flow in this experiment comes from the cases with a coherent oscillation at 6–7 kHz in the poloidal velocity (e.g. sample shot 1110110026), as shown at the bottom right of figure 9. This oscillation, when it occurred, had a near-constant frequency over at least ± 1 cm around the separatrix, as shown in figures 10, 11 and 13, and was correlated with magnetic fluctuations at the same frequency, as shown in figure 14. All shots with this coherent feature had ICRF heating, although shots with somewhat lower ICRF power had no such oscillation (e.g. 1100824014, 1100824015).

Somewhat less clear, but still interesting, are the cases with a broadband intermittent spectrum in the poloidal velocity (e.g. shot 1100120025), as shown at the top right of figure 9. These cases had a complex spectrum in the range ~1–20 kHz which varied with time, but with a radial structure of δV_{pol} which was correlated over about ± 0.5 cm near the separatrix, as shown in figures 11 and 13, which is comparable to the radial scale length of the turbulence. The radial width of the correlation of these poloidal flows had a clear decrease with the line-averaged density, as shown in figure 12. However, in the highest density cases (e.g. shot 1100824017) it was not clear whether the small poloidal fluctuations detected by this analysis were actually large-scale zonal flows, or instead the residual result of averaging over the random small-scale flows due to turbulence.

The most plausible theoretical candidate to explain the coherent oscillations in this experiment is a GAM, such as seen in many previous experiments (see also section 5.6). An approximate formula for the expected frequency of a GAM for a shaped tokamak with aspect ratio A, elongation κ and edge safety factor q is [42]: $f = G c_s/(\pi R)$, where the geometrical factor is $G = 2^{-0.5}(2/(1+k))(1+1/(2A^{2/3}))(1+1/(4q^2))$ and $c_s = [\gamma Z(T_e + T_i)/M_i]^{0.5}$. For C-Mod: $\kappa = 1.6$, $A = 3$, $q = 3.4$, $Z = 1$, $M_i = 2$, and assuming for the shot with a coherent peak in δV_{pol} (1110114026) $T_i = T_e = 150\,eV$ (appropriate for $\rho \sim 0$ cm) and $\gamma = 4/3$, this frequency is $f_{GAM} \sim 34$ kHz. However, there is quite a large variation in T_e (and presumably T_i) over the radial range in which the oscillation is observed; for example, $T_e = 36$–$340\,eV$ for this shot over $\rho = \pm 0.5$ cm (see table 2), which implies a radial frequency variation of $f \sim 17$–52 kHz which is not observed in this experiment. Thus the identification of this mode with a GAM is inconclusive until the radial structure of this mode is understood.

The broadband and intermittent poloidal velocity fluctuations seen in this experiment might be related to the 'zero-mean frequency' zonal flows described by other theoretical models [4]. These flows can have a radial scale length comparable to the turbulence and do not have a single frequency. They can in theory be affected by collisional damping in the edge, which might be related to the increased radial correlation as the line-averaged density decreased (figure 12). Collisional damping is approximated as [4]: $\gamma = \omega_t^2/\nu_{ii}$, where $\omega_t = v_i/qR$ and ν_{ii} is the ion–ion collision frequency. For typical edge parameters for 1100120025 of $T_i \sim 50\,eV$ and $n \sim 4 \times 10^{13}\,cm^{-3}$, this gives $\gamma \sim 5000\,s^{-1}$, which is not inconsistent with the duration of the bursts of flow seen for this shot at the top of figure 9. This dependence might help explain (at least qualitatively) the density dependence shown in figure 12, although the boundary between broadband intermittent zonal-type flows and random turbulence at high density in figure 12 is not yet clear. Another potential explanation for the density dependence of figure 12 is that if the mean density is increased, then the edge density gradient should steepen accordingly. Thus one could interpret the decrease in the radial cross-correlation of δV_{pol} with density

as due to a decrease in the local density gradient scale length L_n, since L_n enters into both drift wave and ITG turbulence scales (although somewhat differently), which determine the radial width of zonal flow structures. Such a trend of decreasing turbulence correlation lengths with increasing density is indeed seen in the data of figure 4.

The coincidence between the coherent poloidal velocity oscillations and magnetic field fluctuations shown in figure 14 is not yet explained. Possible candidates include a poloidal edge velocity oscillation associated with one of the normal low-m MHD modes, a magnetic component of the usual electrostatic GAMs [43], an energetic particle-driven GAM [44–46], or a zonal magnetic field [47]. A few similar observations have been made previously, as discussed in section 5.6.

The results of the data analysis of figures 10 and 11 indicate that both the coherent and the broadband poloidal flow fluctuations can extend from inside the separatrix at $\rho \leqslant -0.5$ cm across the separatrix into the SOL at $\rho \geqslant 0.5$ cm, which is somewhat surprising since the physics clearly changes around the separatrix. In theory, low frequency 'stationary' zonal flows should be strongly damped by parallel motion at the edge of tokamaks [42], and true $m = 0$ flows cannot exist in the SOL. On the other hand, GAMs are known to exist in the edge plasma [6], and can extend past the separatrix if the field lines are allowed to move freely across the wall, because the field lines can move with the poloidal flow without being deformed. Thus the data showing δV_{pol} fluctuations extending across the separatrix may point to their identification with GAMs, rather than with low frequency zonal flows. Another possibility is that the process of blob formation in the near-SOL may generate poloidal flow fluctuations localized near the outer midplane where they are measured in this experiment, such as those seen in the SOL in 2D simulations [48].

In conclusion, there is not yet a clear quantitative connection between the poloidal flow fluctuations seen in this experiment and the theory of zonal flows or GAMs. Such a comparison would benefit from a specific simulation of zonal flows in these C-Mod edge plasmas in L-mode, which has not yet been done.

5.5. Velocity cross-correlations

The zero-time cross-correlations of the poloidally averaged δV_{pol} and δV_{rad} with each other and with the GPI signal fluctuations were shown for the four sample shots in figure 13. These correlations can provide insight into poloidal flow generation and radial transport due to these fluctuations. For example, the Reynolds stress R describes the turbulent generation of poloidal flows, i.e. $R = \mathrm{d}/\mathrm{d}r\langle \delta V_{pol} \delta V_{rad}\rangle = \nu_{damp} V_{pol}$, where ν_{damp} is the damping rate of the poloidal flows generated by this correlation [48–50].

The normalized cross-correlation coefficients $\langle \delta V_{pol} \delta V_{rad}\rangle / (\langle \delta V_{pol}^2 \rangle^{1/2} \langle \delta V_{rad}^2 \rangle^{1/2})$ for the four sample shots were shown at the upper right of figure 13. These results show a significant correlation coefficient (up to ~0.5), but have a complicated and variable radial structure with both positive and negative values. For example. inside the separatrix for shot 1091216030, we can estimate $\langle \delta V_{pol} \delta V_{rad}\rangle \sim -0.3$ at $\rho \sim -0.5$ cm with a local gradient scale length of ~ 0.3 cm; thus assuming a typical value of $V_{rad} \sim -0.1 \pm 0.1$ km s^{-1} for this case (figure 6), we can estimate $\nu_{damp} \sim -0.3 V_{rad}/0.3\,\mathrm{cm} \sim 10^4$ s^{-1}, with a range of at least $\nu_{damp} \sim$ (0–2) $\times 10^4$ s^{-1}. This is within an order-of-magnitude of the collisional damping rate of 5000 s^{-1} estimated in section 5.4, and also of the possible damping due to charge exchange of ions with neutrals, i.e. $\nu_{io} = n_o \langle \sigma v \rangle_{io} = (2 \times 10^{-8}\,\mathrm{cm^3\,s^{-1}})(0.5 \times 10^{12}\,\mathrm{cm^{-3}}) \sim 10^4\,\mathrm{s^{-1}}$, assuming $n_o = 0.5 \times 10^{12}$ cm^{-3} (the actual neutral density is not measured inside the separatrix). Obviously this estimate of the poloidal flow damping is highly uncertain even for this one case, and so a more detailed study is needed in order to understand the poloidal flow generation in this experiment.

The normalized zero-time cross-correlation coefficients $\langle \delta V_{pol} \delta I_{GPI}\rangle$ shown at the lower left of figure 13 are largest for the shot with the near-coherent oscillation in δV_{pol} (1110114026). This suggests that there is a decrease in the turbulence level associated with a positive (i.e. electron diamagnetic drift) velocity fluctuation in this case. A similar correlation was seen in the 'quiet periods' in NSTX [17]. However, in other experiments [7, 26] a 90° phase shift was seen between the turbulence level and the zonal flow (i.e. poloidal velocity fluctuation), similar to a 'predator–prey' relationship. Further investigation of this phase relationship is important but beyond the scope of this paper.

Finally, the zero-time cross-correlation coefficients $\langle \delta V_{rad} \delta I_{GPI}\rangle$ are shown at the lower right of figure 13. These fluctuating quantities are averaged over the poloidal region of interest, and so their correlation measures the 'zonal' component of the radial transport. There was only a small ($\leqslant$0.2) correlation between these quantities in all cases, but this was still well above the expected random cross-correlation of ~1%, and even a small level of this correlation is sufficient to cause significant radial transport. For example, if this cross-correlation is taken to be 0.1, and a typical radial velocity fluctuation level is $\delta V_{rad} \sim 0.2$ km s^{-1} (figure 8), and if the local $\delta n/n$ is assumed to be the same as the GPI fluctuation level $\delta I_{GPI}/I$ of 10% near the separatrix (figure 5) where $n_{edge} \sim 5 \times 10^{13}$ cm^{-3}, then the local particle flux is $\Gamma = \langle \delta V_{rad} \delta n\rangle \sim (0.1)\ (0.1)\ n_{edge} V_{rad} \sim 10^{16}$ particles cm^{-2} s^{-1}. Assuming a surface area for particle loss of $(2\pi R)(2\pi \kappa a) \sim 10^5$ cm^2, the resulting particle loss would be ~10^{21} s^{-1}, which is comparable to expected global loss rate of a C-Mod plasma with an average density of 10^{14} cm^{-3}, a volume of ~1 m^3, and a particle confinement time of 0.1 s. Thus even the small cross-correlation levels of $\langle \delta V_{rad} \delta I_{GPI}\rangle$ in figure 13 could be responsible for a significant radial transport.

5.6. Relationship to results from other experiments

The main new results from this paper concern the time-dependent measurements of the poloidal velocity of turbulence motion in C-Mod in the frequency range ~1–30 kHz. These results are at least qualitatively similar to several results from other experiments, as described below. Note that spectroscopic measurements of plasma velocity using diagnostics such as CHERS are (so far) too slow to evaluate zonal flows in this frequency range.

Coherent fluctuations in edge poloidal velocity in the frequency range ~5–20 kHz have been measured in many tokamaks and identified as GAMs. For example, the poloidal velocities of GAMs have been measured using Langmuir probes in T-10 [21], visible imaging in DIII-D [9], Doppler reflectometry in ASDEX Upgrade [12, 15], and heavy ion beam probes in JFT-2M [11] and JIPPT-IIU [13]. The coherent fluctuations observed here in figures 9-11 for shot 1110114026 are in this frequency range, and the poloidal velocity fluctuation level of ~0.2–0.6 km s^{-1} seen here (figure 6) is similar poloidal velocity fluctuations seen in GAMs, e.g. ~0.2–0.8 km s^{-1} in ASDEX [15]. The present results show these oscillations extend outside the separatrix, which has apparently not been seen previously. The frequency of GAMs in previous results generally increased toward the core, which was not seen here.

A coincidence between the coherent poloidal flow oscillations and edge magnetic fluctuations such as seen in figure 14 was previously observed for GAMs in T-10 [21] and for energetic particle-driven MHD bursts in DIII-D [44] and CHS [46]. It is interesting to note that the coherent oscillation seen here occurred only during discharges with ICRH heating, which presumably had energetic ion tails. These GAM-like fluctuations are steady in frequency (see figures 9 and 15), similar to the combined ICRH and neutral beam heated plasmas in JET [51], though in that case the ICRH was deposited on the high-field side. The final three shots in table 1, 1110114026–32, feature either on-axis or low-field side ICRH deposition. A further indication of energetic ion interactions with the GAM would be energetic ion losses, however, such a connection has not been established.

The time dependence of the amplitude of the coherent $\delta V_{\rm pol}$ oscillations near the L–H transition shown in figure 15 is similar to that seen in ASDEX Upgrade [19], and DIII-D [26], NSTX [17, 18] and TJ-II [7]. In those cases there was an apparent increase in coherent edge $V_{\rm pol}$ oscillations (either GAMs or zonal flows) well before the transition, and a decrease at or just after the transition. The amplitude modulation in $\delta V_{\rm pol}$ at ~0.5 kHz seen in figure 15 during the 10 ms prior to the L–H transition also looks similar to the ~2 kHz 'bursting' (ASDEX Upgrade), 'quiet periods' (NSTX) or 'predator–prey oscillations' (DIII-D) seen in these other devices. However, the nature of the 'trigger' event for the L–H transition is not yet clear from any of these results; presumably, this event occurs on a fast ($\leqslant 100\,\mu$s) timescale, comparable to the fast changes in edge profiles at the final transition. Clearly a larger database of L–H transitions is needed for C-Mod before drawing any definitive conclusions.

Broadband fluctuations in edge poloidal velocity, i.e. 'zero-frequency' zonal flows, have also been measured in a similar frequency range in several tokamaks. For example, broadband low frequency zonal flows were seen with BES in the frequency range ~1–10 kHz in the core of DIII-D [14], and broadband zonal flows were measured with probes in the frequency range 0.5–4 kHz in the edge of HT-7 [10] and HL-2A [22]. Relatively little is known about such fluctuations, so is possible that the broadband $\delta V_{\rm pol}$ spectra such as shown for shot 1100120025 in figures 9-11 are similar to these other experiments. The most interesting characteristic of these fluctuations in the present experiment is the decrease in their radial correlation width with increasing density shown in figure 12, which is qualitatively similar to the decrease in GAM amplitude with density seen in previous experiments, attributed to collisional damping [15].

There have been many previous measurements of edge and SOL radial velocity fluctuations using probes [1–3], which have been used to estimate the local turbulent particle transport $\langle \delta V_{\rm rad} \delta n \rangle$. For example, $\delta V_{\rm rad}$ distributions in the range ~1 km s^{-1} were seen in DIII-D [32] and JET [33] which are at least qualitatively similar to the $V_{\rm rad}$ distributions shown here in figures 8. Note, however, that the $V_{\rm rad}$ calculated here were averaged over the poloidal viewing region of ~5 poloidal correlation lengths, while the previous measurements were more local.

Finally, a separate analysis of the 2D array of GPI diode detectors [52] cites features in C-Mod *I-mode* [53] edge turbulence that are characteristic of zonal flows and that are preliminarily indentified as GAMs. This analysis showed that for $k_{\rm pol}^{\rm ZF} = 0 \pm 1$ cm^{-1} and $f^{\rm ZF} = 20$ kHz, there was a non-linear phase coupling between the 20 kHz mode and higher frequency 'weakly coherent mode (WCM)' present in C-Mod's I-modes.

5.7. *Conclusions and further directions*

This paper described an analysis of poloidal velocity fluctuations in the edge turbulence of Alcator C-Mod as measured by the GPI diagnostic near the outer midplane separatrix. These velocity fluctuations were either coherent at ~6–7 kHz or broadband in the range ~1–20 kHz, and had an amplitude comparable to the mean (i.e. time-averaged) poloidal velocity. We conclude that some of these results are similar to the GAMs and/or zonal flows described in theory and previous experiments, as discussed in detail in sections 5.4 and 5.6.

It is important to note that the zonal flow-like fluctuations seen in this experiment were only measured in a relatively localized region near the outer midplane. Thus an important diagnostic improvement would be to have GPI views at other poloidal and/or toroidal locations in order to look for the large-scale $n = 0$, $m = 0$ nature of the zonal flow, as done previously with other zonal flow diagnostics. Further systematic experiments would be useful to clarify the location in parameter space of the coherent poloidal velocity oscillations, which were seen here only during low density, RF heated plasmas. It would also be interesting to examine more L–H transitions to determine if the relatively large width of the oscillating poloidal flows were somehow causing the transition.

Theory and/or simulations should be done specifically to evaluate zonal flows for plasma parameters of the C-Mod edge. These simulations could help guide further searches for zonal flows in C-Mod, including truly 'zero frequency' modes which are difficult to distinguish from mean flows. Given the observed correlation of the coherent flows with MHD activity, it would also be useful to calculate the magnetic component of such zonal flows, and also the poloidal flows associated with normal MHD activity, in order to clarify this relationship.

Notice

Acknowledgments

The authors thank B Davis, D D'Ippolito, P Diamond, T Golfinopoulos, O Grulke, K Hallatschek, T S Hahm, B LaBombard, D Russell, D Stotler, G Tynan, S Wolfe and Alcator C-Mod Team for their contributions or comments. This work was supported in part by US DOE Contracts DE-AC02-09CH11466 and DE-FC02-99ER5412.

References

[1] Wootton A J *et al* 1990 *Phys. Fluids* B **2** 2879
[2] Zweben S J *et al* 2007 *Plasma Phys. Control. Fusion* **49** S1
[3] Boedo J A 2009 *J. Nucl. Mater.* **390–391** 29
[4] Diamond P H *et al* 2005 *Plasma Phys. Control. Fusion* **47** R35
[5] Tynan G R, Fujisawa A and McKee G 2009 *Plasma Phys. Control. Fusion* **51** 113001
[6] Fujisawa A 2009 *Nucl. Fusion* **49** 013001
[7] Hidalgo C 2011 *Plasma Phys. Control. Fusion* **53** 074003
[8] Stroth U *et al* 2011 *Plasma Phys. Control. Fusion* **53** 024006
[9] McKee G R *et al* 2003 *Phys. Plasmas* **10** 1712
[10] Xu G S *et al* 2003 *Phys. Rev. Lett.* **91** 125001
[11] Hamada Y 2005 *Nucl. Fusion* **45** 81
[12] Conway G D *et al* 2005 *Plasma Phys. Control. Fusion* **47** 1165
[13] Ido T *et al* 2006 *Plasma Phys. Control. Fusion* **48** S41
[14] Gupta *et al* 2006 *Phys. Rev. Lett.* **97** 125002
[15] Conway G D *et al* 2008 *Plasma Phys. Control. Fusion* **50** 085005
[16] Xu G S *et al* 2009 *Nucl. Fusion* **49** 092002
[17] Zweben S J *et al* 2010 *Phys. Plasmas* **17** 102502
[18] Sechrest Y *et al* 2011 *Phys. Plasmas* **18** 012502
[19] Conway G D *et al* 2011 *Phys. Rev. Lett.* **106** 065001
[20] Fujisawa A 2004 *Phys. Rev. Lett.* **93** 165002
[21] Melnikov A V *et al* 2006 *Plasma Phys. Control. Fusion* **48** S87
[22] Liu A D *et al* 2009 *Phys. Rev. Lett.* **103** 095002
[23] Kramer-Flecken A *et al* 2009 *Plasma Phys. Control. Fusion* **51** 015001
[24] Xu Y *et al* 2011 *Plasma Phys. Control. Fusion* **53** 095015
[25] Silva C *et al* 2011 *Nucl. Fusion* **51** 063025
[26] Schmitz L *et al* 2011 private communication
[27] Terry J *et al* 2005 *J. Nucl. Mater.* **337–339** 322
[28] Grulke O *et al* 2006 *Phys. Plasmas* **13** 012306
[29] Zweben S J *et al* 2011 *J. Nucl. Mater.* **415** S463
[30] Czeigler I *et al* 2010 *Phys. Plasmas* **17** 056129
[31] Agostini M *et al* 2011 *Nucl. Fusion* **51** 053020
[32] Boedo J A *et al* 2001 *Phys. Plasmas* **8** 4826
[33] Goncalves *et al* 2005 *J. Nucl. Mater.* **337–339** 376
[34] see http://www.pppl.gov/∼szweben/CMod2010/CMod2010.html
[35] Stotler D P *et al* 2003 *J. Nucl. Mater.* **313–316** 1066
[36] Stotler D P *et al* 2007 *J. Nucl. Mater.* **363–365** 686
[37] Zweben S J *et al* 2004 *Nucl. Fusion* **44** 134
[38] Zweben *et al* 2009 *Phys. Plasmas* **16** 082505
[39] Munsat T and Zweben S 2006 *Rev. Sci. Instrum.* **77** 103501
[40] Holland C *et al* 2004 *Rev. Sci. Instrum.* **75** 4278
[41] Maqueda R J *et al* 2009 *Phys. Plasmas* **16** 056117
[42] Hallatschek K 2007 *Plasma Phys. Control. Fusion* **49** B137
[43] Hallatschek K and McKee G 2011 *EPS Meeting (Strasbourg, France)* P.2132
[44] Nazikian R *et al* 2008 *Phys. Rev. Lett.* **101** 185001
[45] Fu GY 2008 *Phys. Rev. Lett.* **101** 185002
[46] Ohshima S *et al* 2007 *Plasma Phys. Control. Fusion* **49** 1945
[47] Fujisawa A *et al* 2007 *Phys. Rev. Lett.* **98** 165001
[48] Russell D A *et al* 2009 *Phys. Plasmas* **16** 122304
[49] Tynan G R *et al* 2009 *Plasma Phys. Control. Fusion* **51** 124055
[50] Windisch T *et al* 2011 *Plasma Phys. Control. Fusion* **53** 085001
[51] Berk H L *et al* 2006 *Nucl. Fusion* **46** S888
[52] Cziegler I 2011 *PhD Thesis* MIT
[53] Hubbard *et al* 2011 *Phys. Plasmas* **18** 056115